2017

Characterization of mechanical properties in nanoparticle reinforced hybrid carbon fiber composites using photoluminescence piezospectroscopy

Sanjida Jahan
University of Central Florida

STARS Citation

Jahan, Sanjida, "Characterization of mechanical properties in nanoparticle reinforced hybrid carbon fiber composites using photoluminescence piezospectroscopy" (2017). *Electronic Theses and Dissertations, 2004-2019*. 5666.
https://stars.library.ucf.edu/etd/5666

CHARACTERIZATION OF MECHANICAL PROPERTIES IN NANOPARTICLE REINFORCED HYBRID CARBON FIBER COMPOSITES USING PHOTOLUMINESCENCE PIEZOSPECTROSCOPY

by

SANJIDA AKTER JAHAN
B.S. Military Institute of Science and Technology, 2013

A thesis submitted in partial fulfilment of the requirements
for the degree of Master of Science
in the Department of Mechanical and Aerospace Engineering
in the College of Engineering and Computer Science
at the University of Central Florida

Fall Term
2017

Major Professor: Seetha Raghavan

ABSTRACT

Carbon fiber composites have become popular in aerospace structures and applications due to their light weight, high strength, and high performance. Hybrid carbon fiber reinforced polymer (HCFRP) composites with alumina nanoparticles reinforcement display improved material properties such as fracture toughness, resistance to crack propagation and improved fatigue life. However, homogeneous dispersion of nanoscale materials in the matrix is important for even distribution of the improved properties. Implementing silane coupling agents (SCAs) improves dispersion by acting as a bridge between organic and inorganic materials, which increases interfacial strength and decreases sedimentation by bonding the particulate filler to the fiber reinforcement. This research is aimed at quantifying the improvement in dispersion of nanoparticles and elucidating the effects on the mechanical property of HCFRP samples through the novel use of photoluminescent characteristic peaks emitted by the alumina reinforcement particles. Photo-luminescene emission from secondary reinforcement particles of alumina embedded within the hybrid carbon fiber composites is leveraged to reveal microstructural effects of functionalization and particle weight fraction as it relates to overall composite mechanics.

6, 9 and 12 weight percentage of alumina particle loading with Reactive Silane Coupling Agents, Non-reactive Silane Coupling Agent surface treatments and untreated condition are investigated in this research. Uniaxial tensile tests were conducted with measurements using piezospectroscopy (PS) and concurrent digital image correlation (DIC) to quantify the mechanical property and load distribution between the carbon fiber/epoxy and the reinforcing nanoparticles. The piezospectroscopic data were collected in an in-situ configuration using a portable piezospectroscopy system while the sample was under tensile load. Photoluminescence results show the dispersion and sedimentation behavior of the nanoparticles in the material for different surface treatment and weight percentage of the alumina nanoparticles. The piezospectroscopic maps capture and track the residual stress and its change under applied load. The results reveal the effect of varying particle loading on composite mechanical properties and how this changes with different functionalization conditions. The role of the particles in load transfer in the hybrid composite is further investigated and compared with theory. This work extends the capability of spectroscopy as an effective non-invasive method to study, at the microstructural level, the material and manufacturing effects on the development of advanced composites for applications in aerospace structures and beyond.

”You can’t cross the sea merely by standing and staring at the water.”

- Rabindranath Tagore

ACKNOWLEDGMENTS

My exceeding thanks to my family for supporting me through this journey, to my research advisor and Thesis Chair, Dr. Seetha Raghavan, for support and guidance on the project, to my committee members Dr. Jihua Gou and Dr. Yuanli Bai for their participation, and continued support. To my colleagues at the University of Central Florida who assisted in the project. This work was supported by University of Central Florida's International Affairs and Global Strategies in-house grant.

TABLE OF CONTENTS

LIST OF FIGURES

LIST OF TABLES

CHAPTER 1: INTRODUCTION

Motivation and Background

The future of aerospace structures is highly dependent on the advancement of reliable and high performing materials [6]. One group of high performing materials includes carbon fiber composites, which have become widely used in aerospace applications due to their high strength to weight ratios [7]. Specifically, hybrid carbon fiber reinforced polymer (HCFRP) composites are a growing area of interest for aerospace researchers, since they provide advanced tailoring and improved mechanical properties [8, 9].

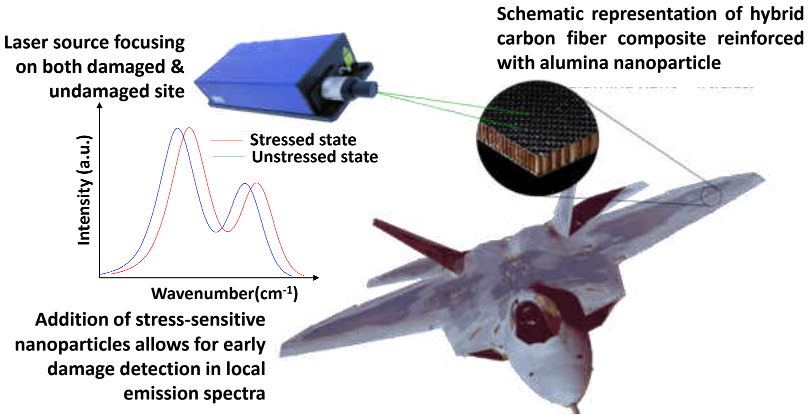

Figure 1.1: Applications of hybrid carbon fiber composites for aerospace applications, improving material properties and allowing for stress sensing

Certain hybrid composites can be engineered to not only provide improved mechanical properties, but also provide multi-functionality through inherent sensing capabilities. Hybrid carbon fiber alumina nano-composites provide improvements in mechanical properties [10, 11, 12] and has the potential to offer non-contact stress sensing capabilities through the alumina nanoparticles inherent photo-luminescent piezospectroscopic properties [13, 14, 15]. The research challenge that presents itself here is one where both functions must be optimized with the appropriate configurations of materials and property parameters. Here, the goal is to design these composites with enhanced sensing capability from the photoluminescence characteristics while maintaining the capacity of improved mechanical properties, namely fracture toughness. A successful configuration of parameters will enable structures with superior toughness and added sensing properties that report structural integrity.

In this research effort, in order to study the stress sensing abilities of the alumina HCFRP, three varying HCFRP panels were manufactured with alumina nanoparticles at 6, 9 and 12 weight percent content, through a technique known as resin infusion under flexible tooling (RIFT). For better dispersion and reduced sedimentation and agglomeration, alumina nanoparticles were treated with two silane coupling agents i.e. reactive silane coupling agent (RSCA) anf non-reactive silane coupling agent (NRSCA). At pre-determined static tensile holds, photo-luminescence maps were obtained from the front surface in order to study the piezospectroscopic stress sensing ability of the material, and digital image correlation (DIC) images were simultaneously captured on the back surface to track and compare strain distribution in the material. The photo-luminescent mapping technique was also used to study the dispersion of nanoparticles of each surface of the composites [1].

Applications of Piezospectroscopy in Material Characterization

Applications using the piezospectroscopic technique began with the widespread use of the R1 line to monitor pressure in diamond anvil cells [16] followed by the determination of stresses in polycrystalline ceramics [17, 18, 19] and alumina-filled composites for electronic applications [20]. The method gained importance over the last two decades as a means to assess the integrity of the thermally grown oxide (TGO) layers of thermal barrier coatings [21, 22, 23, 24] on jet engine turbine blades. An ex-situ photo-luminescence spectroscopy study was conducted to investigate the stresses within the thermally grown oxide of a thermal barrier coating in complex realistic conditions, such as induced thermal gradients, and long duration aging [3]. The resulting high spatial resolution stress contour maps highlight the development of the thermally grown oxide in response to the complex conditions. But the stress induced in the structure was not large enough to determine the piezospectroscopic coefficient for the system.

In further work, a novel method to verify the particle dispersion and volume fraction in alumina-epoxy nanocomposites using PSLS was presented. The application of this method as a quality control technique can greatly improve the manufacturing of these nanocomposites and, therefore, ensure optimal properties are achieved in applications in which the addition of nanoparticles to an epoxy or polymer are used to improve the mechanical properties [1]. A uniaxial compression test was conducted to determine the piezospectroscopic coefficient for the alumina-epoxy nanomaterials for different volume percentages and with highest compressive stress of 120 MPa, the frequency shift measured was 0.7 cm^{-1} [14].

The potential to monitor real-time stress evolution with high, multi-scale spatial resolution was demonstrated using piezospectroscopy and verified through direct comparison with DIC [25]. The stress-sensing behavior of alumina-epoxy nanoparticle coating was applied to a composite substrate in an open hole tension configuration and validated with the biaxial strain field concurrently determined through digital image correlation. The coating achieved early detection of composite failure initiation and subsequently tracked stress distribution in the immediate vicinity of the crack as it progressed, demonstrating non-invasive stress and damage detection with multi-scale spatial resolution [25].

A quick and comprehensive technique to quantify dispersion of particles in hybrid composites using photoluminescence property of embedded particle was developed by Hanhan et al [2]. In this work, the technique is being used to quantitatively determine load distribution on the alumina particles. The piezospectroscopic property of alumina particles under mechanical load allows the determination of the load carrying contribution of the particles and a better understanding of the reinforcing mechanism. In further work, silane functionalization was introduced to improve the dispersion of the nanoparticles and reduce agglomerations which adversely affect material properties [26].

Hybrid Carbon Fiber Reinforced Polymer Composites (HCFRPs)

Hybrid carbon fiber reinforced polymer (HCFRP) composites consist of carbon fiber reinforcements with a particulate filler, a secondary reinforcement which provides enhanced hybrid properties [27]. HCFRPs are promising materials that utilize these reinforcements to increase the crack initiation toughness [28], increase fracture toughness [29], and improve tensile elastic modulus [30]. However, dispersion of the reinforcing particles affects these improvements. Uniformity of the reinforcement distribution offers much better mechanical performance [31]. The use of sonication in processing is one of many methods that improves the dispersion [32]. It is not an easy task to achieve homogeneous dispersion of nanoparticles because of the challenges in phase separation and agglomeration [33]. To mitigate the these adverse effects, a number of functionalization techniques are being used. Silane coupling agents originated as surface treatments used to strengthen the interface between fiber and matrix in glass fiber reinforced polymer composites [34]. Recent work has shown improvements in the dispersion of alumina nanoparticles within a polymer matrix, improving elastic modulus and tensile strength, through surface modifications with silane coupling agents [35]. The improvement in dispersion of particles arises from the reduced particle to particle interactions that contribute to agglomeration [36]. In addition to providing for improved particle dispersion, the chemical bonding of the particulates to the matrix can also provide for a higher particle-matrix interfacial strength when compared to unmodified particles [37]. Another type of particle surface treatment known as non-reactive coupling agents are also explored due to their benefits in improving particle dispersion through decreasing particle surface tension which in turn decreases particle interactions at the potential cost of a weakened particle/matrix interface [38].

Researchers have been investigating many ways to quantify the improvement in dispersion of nanoparticles due to its significance in different fields. One study used the traditional method of micrographs to classify the dispersion-quality of nanoparticle composites [39]. Also, quantitative dispersion characterization method [40] and wide angle X-ray scattering method have been used to characterize the performance of nanocomposites with respect to their morphological configuration [41]. Characterizing the consequence of non-homogeneous reinforcement distribution on the mechanical properties of these materials is still important. Secondary reinforcement particles of alumina embedded within the hybrid carbon fiber composites have an additional photoluminescent property that allows measurements to provide dispersion and stress results from characteristic peaks emitted by the particles [42, 43, 44] and this has been the focus of our research. Figure 1 represents a schematic for application of HCFRPs in aerospace industries and the stress sensing capability of alumina embedded HCFRPs.

Overview of Research

An examination of non-destructive testing techniques for application in determining material readiness for commercial application, providing in-situ measurements for remote testing, and non-invasive examinations of sensitive equipment is of great interest to both industry and the research community. Analysis of material properties and loading response under working conditions can provide valuable information for advancing novel materials application into industry. Currently, a lack of material properties and response under loading conditions limit our understanding of mechanical behavior of the hybrid carbon fiber reinforced polymer composites. Herein a discussion of the motivation behind the research is presented, aimed at the introduction of multi-functionality in fiber composites. An overview of non-destructive characterization is developed. In Chapter 2 an introduction to the theory and measurement methods is detailed, including Photoluminescence Spectroscopy and piezospectroscopy. Data analysis and fitting procedures for developing particle dispersion and stress behavior is also outlined. Chapter 3 describes the application of nanoparticle reinforcement as well as using alumina as a reinforcement including its silane functionalization technique. The specimen materials, geometry, and experimental setup are detailed in Chapter 4. Specimen manufacturing and methodology of loading and measurements techniques are described. A combination of non-destructive testing techniques on the materials is discussed. Dispersion and piezospectroscopic results from the experiment along with DIC results are presented in Chapter 5, including the findings from the dispersion and the piezospectroscopic maps. In Chapter 6 the conclusions and future outlook of these non-destructive testing methods will be discussed.

CHAPTER 2: PIEZOSPECTROSCOPY METHOD

Photoluminescence Mechanisms in Alumina

The photoluminescence phenomenon occurs in alumina through the excitation of trace chromium ion impurities. Investigations into the photoluminescenct emissions originated with pressure measurements in diamond anvil cells [45] and stress measurements in the thermally grown oxide layer of thermal barrier coatings [46]. Recent work has utilized this technique for the characterization of stress and dispersion behavior of composites systems with alumina reinforcement [14, 2, 47].

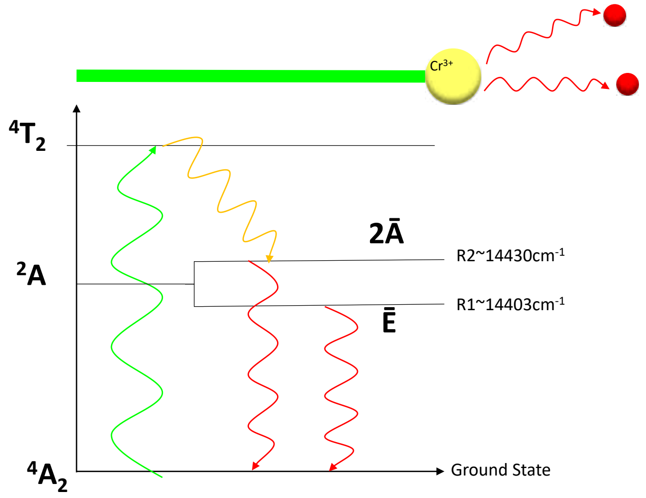

Figure 2.1: Electron diagram showing energy levels associated with Al_2O_3 photoluminescence [1]

The photoluminescent properties of alumina are generated from the chromium (Cr^{3+}) substitutional impurities [48]. These impurities occupy sites with trigonal distortion. When these chromium impurities are excited with a laser, the material emits photons that are distributed in the shape of the characteristic R-line doublet. This results from the photoluminescence phenomenon, a schematic of which is presented in Figure 2.1. Photoluminescence is defined as a non-equilibrium emission of radiation caused by a photon excitation [49]. This radiation, from the Cr^{3+} ions, occurs as a transition from the lowest energy excited state (^2E_g) to the ground state ($^4A_{2g}$) of the ion [50]. This transition is highly unlikely because of a spin flip requirement, being a change from a doublet to quartet energy state, which prevents a direct excitation from the ground state to the ^2E_G energy level. The photoluminescence mechanism in alumina therefore necessitates a nonradiative transition from higher energy quartet states ($^4T_{1g}$ and $^4T_{2g}$) to the ^2E_g state. The distortion present at the substitution site provides for a splitting of the ^2E_g energy level into an $\bar{E}$ and a $2\bar{A}$ energy state which results in the doublet emissions [50].

Photoluminescence Piezospectroscopy

Investigations regarding the evolution of the piezospectroscopic effect (PS) and the corresponding theoretical principles in alumina materials ($Al_2O_3Cr^{3+}$) is extensive. A shift in the characteristic R-lines of α-alumina results when the crystal field that encompasses the chromium (Cr^{3+}) ions within the alumina distorts due to applied stress, causing a change in the energy of the electronic transfers [51, 52]. Gaining popularity as the first laser material, ruby (Cr^{3+}-doped sapphire) crystals were studied and applied to a variety of applications including the elucidation of the crystal field theory of ruby luminescence [53]. Modifying the theoretical models for the PS effct, Forman [54] developed the following relationship between the frequency shift of the R-lines and hydrostatic stress:

$$\Delta\nu = \pi\sigma_H \tag{2.1}$$

where σ_H is the hydrostatic stress and π represents the PS coefficient. Furthermore, by averaging over many grains at random orientation, He and Clarke [29] introduced a reduced polycrystalline model given by

$$\Delta\nu = \frac{1}{3}\pi_{ii}\sigma_{ii} \tag{2.2}$$

where π_{ii} is the trace of the experimentally measured PS coefficient tensor and $\frac{1}{3}\sigma_{ii}$ is the hydrostatic stress. In this work, the peak shift over many randomly oriented grains from many nanoparticles, $\Delta\nu$, is measured using the novel Portable Piezospectroscopy System [4], and correlated to the stress applied by the mechanical testing system, as well as to the strain measured via digital image correlation (DIC). Therefore, the piezospectroscopic (PS) coefficient, is given as a typical measure of the stress sensitivity in units of cm^{-1}/GPa [55, 29, 14]. Recent measurements from the piezospectroscopic calibration of alumina-epoxy nanocomposites, presents piezospectroscopic coefficients for three different volume percentages [5]. The piezospectroscopic coefficients were determined for compressive stress and the coefficient varied from 3.16 to 5.63 cm^{-1}/GPa for 5 to 38 vol%.

Photoluminescence Collection and Fitting Methods

For the collection and processing of photoluminescent emissions, it is necessary to utilize several systems. For this work, photoluminescent emissions were captured using a portable piezospectroscopy system. The system utilized for collection of large area photoluminescent emissions combined several different optical systems. A MATLAB® program [55], based on a least squares fitting function is utilized for processing. Preprocessing steps [56] are required in order to prepare the least squares algorithm for doublet fitting. The first process performed is the sectioning of the data. The frequencies included in the raw data generally contain excess information that can distort the least squares fitting process. As a result, points are selected where the derivative of the R-line tails is equal to zero. Data outside of this range is removed, leaving just the desired R-line spectrum. The bounds are also used to define the baseline. This baseline intensity can then be removed through linear fitting. The result of the final step is the determination of the initial guess for the R1 and R2 pseudo-Voigt functions. Using an estimation of the fitted peaks from the raw data, the initial guesses for the full width at half maximum (FWHM), peak position, area under the curve, and Gaussian ratio for both peaks of the doublet are determined.

The pseudo-Voigt functions used to fit both peaks of the doublet are a convolution of Gaussian and Lorentzian line-shapes and have been shown to be an accurate function for the fitting of symmetric peaks [57]. This function assumes that the line-widths of Gaussian and Lorentzian components are equal and is represented as follows [55]:

$$\Phi(\nu) = 2A[\Phi_G(\nu) + \Phi_L(\nu)] \tag{2.3}$$

The $\Phi(\nu)$ term is the combined function, the $\Phi_G(\nu)$ term is the Gaussian function, and the $\Phi_L(\nu)$ term, is the Lorentzian function, and A is the integrated intensity under the spectral function. The Gaussian and Lorentzian functions are shown in Equations 2.4 and 2.5 respectively [55].

$$\Phi_G(\nu) = \frac{GR}{W}\sqrt{\frac{ln2}{\pi}}exp(-4ln2(\frac{\nu - C}{W})^2) \tag{2.4}$$

$$\Phi_L(\nu) = \frac{LR}{\pi W[1 + 4(\frac{\nu - C}{W})^2]} \tag{2.5}$$

For both Gaussian and Lorentzian functions, W is the FWHM, A is the area under the curve, and C is the peak position. The GR term in Equation 2.4 represents the Gauss Ratio, which represents the contribution of the Gaussian lineshape to the pseudo-Voigt function, and is related to the Lorenz Ratio (LR) by $GR = 1 - LR$. The R1 and R2 pseudo-Voigts are combined in Equation 2.6 to represent the R-line doublet function which contains 8 variables (4 variables for each pseudo-Voigt) [55]. Relationships between R1 and R2 variables based on applied load exist and are used to set the upper and lower bounds in order to tie the physical phenomena with the curve fitting algorithm [56, 58].

$$\Phi_{doublet}(\nu) = \Phi_{R1}(\nu) + \Phi_{R2}(\nu) \tag{2.6}$$

Dispersion Analysis Process

Photoluminescence measurements are a promising alternative to traditional dispersion analysis methods. These traditional methods involve processing of micrographs into binary images, where particles can be computationally resolved, allowing for characterization of agglomeration behavior [59, 60]. However, these techniques have limitations arising from micrograph quality. These occur from unclear particle boundaries in addition to the presence of hidden particles [61] not clearly resolved. As such, for the large scale characterization of dispersion behavior it is necessary to utilize a different technique.

Photoluminescence spectroscopy was developed in work preceding this for the characterization of dispersion in polymer nanocomposites [5]. With this technique, the intensity of photoluminescence emissions are compared across a scanning regions. Locations with higher intensity emissions have higher alumina concentrations. Significant deviations in surface intensity distributions are indicative of poor particle dispersion. This method was utilized in order to characterize dispersion in hybrid carbon fiber composites [2], and is further developed in order to provide for quantitative analysis of intensity distributions for determination of optimal dispersion behavior. An example of a photoluminescent map with a schematic of local data is presented in Figure 2.2.

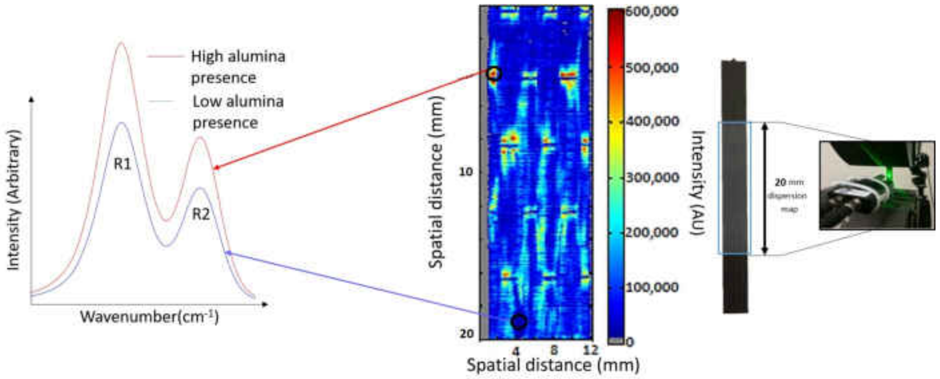

Figure 2.2: Photoluminescence intensity map with data schematic showing local variations in intensity corresponding to particle dispersion[2]

In Figure 2.2, the locations with high alumina nanoparticles have higher R1 and R2 intensity compared to the locations with lower alumina particles. Each point in the contour map represents amount of alumina nanoparticles present at that point. Material properties such as, agglomerations, low particle concentration at the stitching area are also recognizable in the dispersion map[2].

Piezospectroscopic Analysis

This technique can similarly be applied to the mapping of stress across a sample surface. Work preceeding this has utilized digital image correlation and piezospectroscopy for the analysis of carbon fiber samples coated with a non-reinforcing stress sensing coating undergoing open hole tension tests [25]. It was found that this technique provided for earlier crack detection when compared to DIC. This technique can provide for unique measurements of internal composite stresses in different local regions. Embedding of nanoparticles within the carbon fiber composite allows for measurements of load transfer from matrix to particles, which can be extrapolated to provide overall composite load transfer behavior [62]. This stress sensitivity occurs alongside the mechanical property reinforcement through nanoparticle reinforcement. For the work presented, piezospectroscopy is utilized in order to characterize residual stress resulting from sample manufacturing and load contribution to the applied stress in the embedded nanoparticles. A peakshift map is presented in Figure 2.3 with schematics of shifted R-line corresponding to stress variations experienced across the sample surface. This type of peakshift map has been used to describe the stress distributions from the thermally grown oxide(TGO) in thermal barrier coating(TBC) [3]

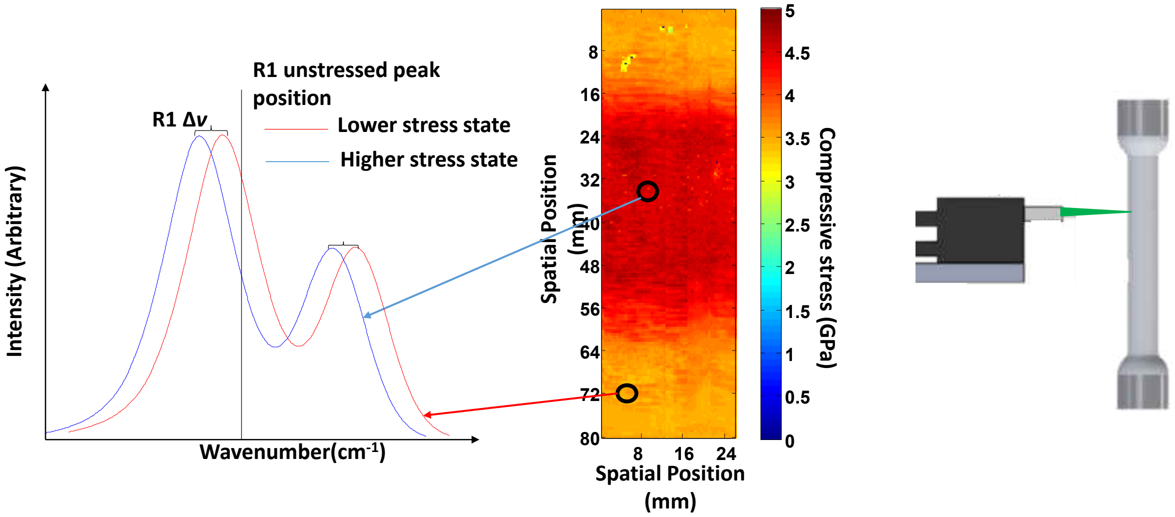

Figure 2.3: Surface peak shift maps show stress distributions in TBC sample from mechanical loading [3]

It is significant to note that the peakshift map is a representation of stresses specifically from the alumina on a multiphase sample. Figure 2.3 demonstrates how the stresses in the specific alumina TGO can be distinguished from other TBC layers. Similarly, data from HCFRP samples showing peakshift will directly represent the stress only within the alumina. This enables the observation of a single phase from a three phase material. The results enable a unique insight into the load transfer amongst the three phases within the HCFRP.

CHAPTER 3: FUNCTIONALIZATION OF HYBRID CARBON FIBER REINFORCED POLYMER COMPOSITES

Nanoparticle Reinforcement

Carbon fiber composites hybridized with alumina nanoparticles are promising next generation materials offering improved properties such as fracture toughness [63], crack initiation toughness [31], and elastic modulus [43] among others [64, 65]. However, these benefits are highly dependent on the homogeneous dispersion of the added nanoparticles [32]. Increasing volume fraction of nanoparticle inclusions results in the presence of agglomerations which act as stress concentrators [66] acting to promote earlier failure. Implementing silane functionalization has been shown to improve material properties by reducing particle agglomeration and creating an even distribution of the particles which further improves mechanical properties of the material [37, 67]. The measurements from photoluminescence spectroscopy provide a unique way of quantifying these improvements through dispersion measurements from functionalization and bonding information from peakshifts. Here the scientific basis for the effects of functionalization is described and how this is related to the physical basis of the effect on dispersion and agglomeration. This allows for an understanding how the spectroscopy results presented in later chapters correlate with the physical mechanisms of functionalization.

Al_2O_3 *as a Reinforced Nanoparticle*

Carbon fiber composites are desirable materials for aerospace applications due to their high strength to weight ratio [7]. However, the two component nature of these materials limits property optimizations as manufacturers are forced to select properties on a linear spectrum of possible values [68].

The introduction of a secondary matrix reinforcement provides for a greater spectrum of selectable material properties. Alumina particles are promising as a secondary reinforcement due to their potential for improvement of mechanical properties such as elastic modulus and fracture toughness [69].

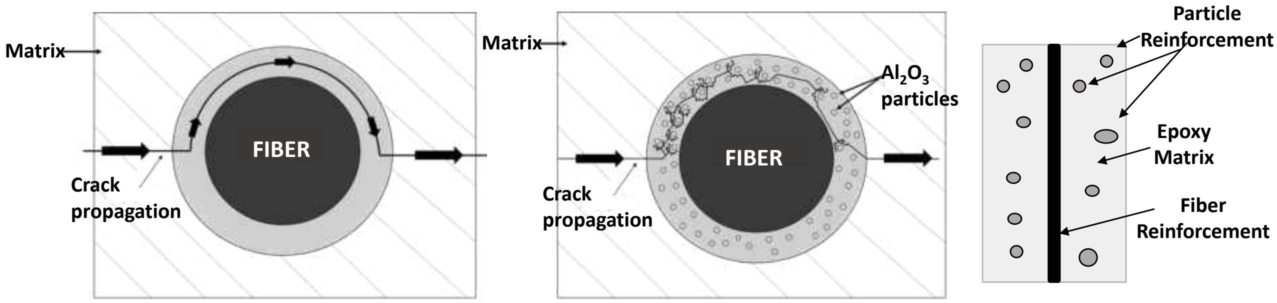

Figure 3.1: The secondary reinforcements increase toughness by shear band yielding resulting in resisting crack propagation

Inclusion of secondary particles have been shown to provide for increases in microcrack stress, interlaminar shear strength, and transverse strength in fiber composites [70]. Improvements to composite flexural and interlaminar shear strength results from toughening of the matrix combined with increased roughness at the surface of the fiber-matrix interface; improvements to fracture toughness results from increased crack deflection due to the secondary reinforcement [10]. This crack deflection mechanism, shown in Figure 3.1, also results in improved tensile modulus and strength [71].

Dispersion and Agglomeration of the Nanoparticles

Polymers reinforced with nanoparticles are desirable due to their unique properties and reinforcing effects. Nanoparticles offer high surface energies, due to a high surface area to volume ratio, which greatly improves mechanical properties when compared to bulk material [72]. However, this high surface energy leads to high particle attractive forces resulting in agglomerations which decrease composite strength [69]. Polymer composites with a large presence of agglomerations have decreased polymer density and an increased polymer chain radius of gyration [73] when compared to polymer composites with the same volume fraction of well dispersed particles, which negatively impacts stiffness. In addition to weakening the polymer through adjusting the morphology, particles act as stress concentrators which further weaken mechanical properties [66]. To maximize the benefits of the incorporated nanoparticulate filler, it is necessary to optimize manufacturing parameters for the reduction of particle agglomerates. This can be done through adjusting manufacturing methods or application of components which mitigate agglomerate formation.

Surface Treatment with Silane Coupling Agents

Silane coupling agents (SCAs) are chemicals which serve to improve bonding of an organic matrix to a dissimilar material, such as an inorganic nanoparticulate filler [74, 75]. Implementing silane coupling agents (SCAs) improves dispersion by acting as a bridge between organic and inorganic materials, which increases interfacial strength and decreases sedimentation by bonding the particulate filler to the fiber reinforcements [67, 76]. This study focuses on two types of coupling agents, reactive silane coupling agent (RSCA) and non-reactive silane coupling agent (NRSCA). RSCAs create a covalent bond between the particle and matrix. NRSCAs do not react chemically and results in reduced surface tension [32].

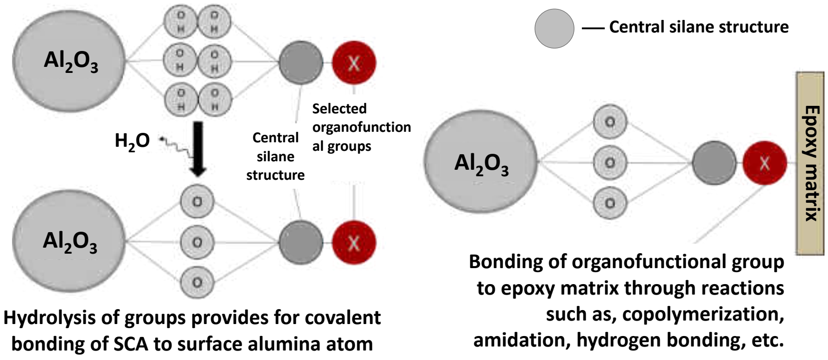

Figure 3.2: Organofunctionality of silane coupling agents (SCAs) improves dispersion in nanocomposites

A schematic for the mechanisms of SCAs is shown in Figure 3.2. The mechanism for SCA bonding to mineral surfaces is a hydrolysis process which creates silanol groups through hydrolyzable group intermediaries for bonding to mineral surfaces [36]. The organofunctionality of these materials is unlocked through the selection of organofunctional groups compatible with the polymer matrix. For the materials tested in this work, an epoxy-functional silane compound is selected to react with the epoxy matrix. These materials are created through either the epoxidation of unsaturated silanes or through the addition of silanes to unsaturated epoxides [77]. These epoxide groups react with epoxide groups from the matrix to form a strong covalent bond.

Reactive bonding from the particles to the matrix has the potential to reduce overall mechanical properties through prevention of particle-matrix debonding, which is a mechanism for accommodating large plastic strains, causing earlier failure in the composite [78]. This behavior is dependent on the stiffness of the particle-matrix interphase, and selection of proper coupling agents can mitigate this failure mechanism. In addition to facilitating mechanical reinforcement, the silane coupling agent also has the potential to improve the stress sensing properties of the alumina nanoparticles within the composite through a strengthened interface. Previous work noted a maximum particle stress indicative of particle-matrix debonding, ultimately decreasing the efficacy of the PS technique at higher loads [39]. A stronger interface providing improved composite load transfer to the particles allows for accurate stress measurements at loads reaching composite failure.

A distinct class of silane coupling agents are also explored in this work. These agents are referred to as non-reactive silane coupling agents (NRSCAs), and are termed such based on the incompatibility of the organofunctional groups with the matrix [79]. As a result, covalent bonding does not occur and adhesion is dominated through weak Van der Waals interactions. While interface strength is greatly lower when compared to reactive coupling agent treatments, these treatments still provide benefits. The lack of covalent bonding is reported to provide lower polymerization stresses [79]. Improvements to particle dispersion is also reported due to a reduction in particle interactions from reduced surface tension; however this decreases particle-matrix interactions which can ultimately decrease material properties [38].

The modification in bonding that occurs with the implementation of the SCAs is shown to be quantifiable through piezospectroscopic measurements in this work. These results provide microstructural information on the local effects on agglomeration and dispersion. The overall effects of SCAs on dispersion are quantified through dispersion maps.

CHAPTER 4: MATERIALS AND EXPERIMENTAL SETUP

Material Manufacturing

The hybrid carbon fiber samples investigated in this work were manufactured by collaborators at Imperial College London and are a combination of three components: being the alumina nanoparticles, carbon fibers, and polymer matrix. These samples were manufactured through a technique known as resin infusion under flexible tooling (RIFT) [27]. A total 18 samples of 9 combinations as shown in Table 4.1 were prepared for the test.

Table 4.1: All combinations of manufacturing parameters for the creation of 9 unique samples

	6 wt%	9 wt%	12 wt%
Untreated	x	x	x
NRSCA treated	x	x	x
RSCA treated	x	x	x

Nanoparticle/Polymer Mixture

To allow for measurements based on photoluminescence, alumina nanoparticles were included as a secondary filler in the carbon fiber composites. The nanoparticles used were α-alumina with an approximate grain size of 40 nm and an average particle size of 150 nm [80]. These were supplied as a powder by Inframat Materials LLC, Connecticut, USA. The epoxy matrix was Epikote 862 (a Bisphenol F and epichlorohydrin based resin) cured with a stoichiometric quantity of Epikure 3402 (an aromatic di-amine based curing agent) supplied by Momentive Materials, Bolton, UK.

Silane coupling agents were applied as surface coatings to the nanoparticles in order to improve the dispersion prior to the processing. Two different types of silane coupling agents were used, supplied by Sigma-Aldrich, Gillingham, UK. γ-glycidoxypropyltrimethoxysilane was used as a reactive silane coupling agent (RSCA) and γ-glycidoxypropyltrimethoxysilyl was used as a non-reactive silane coupling agent (NRSCA). The reactivity of the surface treatments relates to their interactions with the epoxy matrix. The RSCA reacts chemically with the matrix via its amino groups and the epoxide groups of the matrix. The NRSCA treatment does not have the compatible organofunctional groups needed for matrix bonding. Both treatments contain the necessary silanol groups to react with hydroxyl groups in order to bond covalently with the surface of the alumina nanoparticles.

The alumina nanoparticle-resin mixture was prepared in an as-required batch process whereby the necessary quantity of nanoparticles was weighed into a large beaker. The silane coupling agent was then added directly to the particles and the mixture was stirred by hand until complete wetting of the particles was observed. The epoxy resin was then added to the system and stirred for 15 minutes at 150 rpm at a processing temperature of 50°C. Following this, the mixture was homgenized using an ultrasonic processor (Cole Parmer, London, UK). This process improves dispersion of particles suspended in a liquid solution through ultrasonic vibrations. These vibrations cause cavities to form in the mixture and upon their collapse provide a force which is capable of breaking up large particle agglomerations and dispersing particles more evenly throughout the solution [81]. The samples were sonicated for 1 hour in batches of 250 ml. The process generates significant levels of heat and thus the sonication was carried out with the mixture partially submerged in an ice-bath to prevent excessive temperature rises, which would degrade the resin. The particles in the sonicated mixture were observed to remain in suspension over a number of days. Following the sonication, the nanoparticle-resin mixture was thoroughly degassed in a vacuum chamber at a temperature of 50°C. Finally, a stoichiometric quantity of hardener was added, mixed mechanically for 15 minutes and degassed.

Infusion of Carbon Fibers

Unidirectional carbon fiber sheets (UT-C400, Marineware, UK) with a tow size of 12k were used for all composite manufacture [82]. The samples were manufactured using resin infusion under flexible tooling (RIFT) with the fiber direction parallel to the direction of flow of the polymer [83]. Eight plies of carbon fiber were laid up and this produced a carbon fiber plate with a nominal thickness of 3 mm. RIFT is an effective method that allows for the infusion of the nanoparticle-resin mixture and provides for a relatively void-free composite. Alumina weight fractions of the matrix were maintained at values of either 6, 9, or 12 wt% in the resin. The samples were cured for four hours at 120°C with a post cure for a further four hours at 170°C.

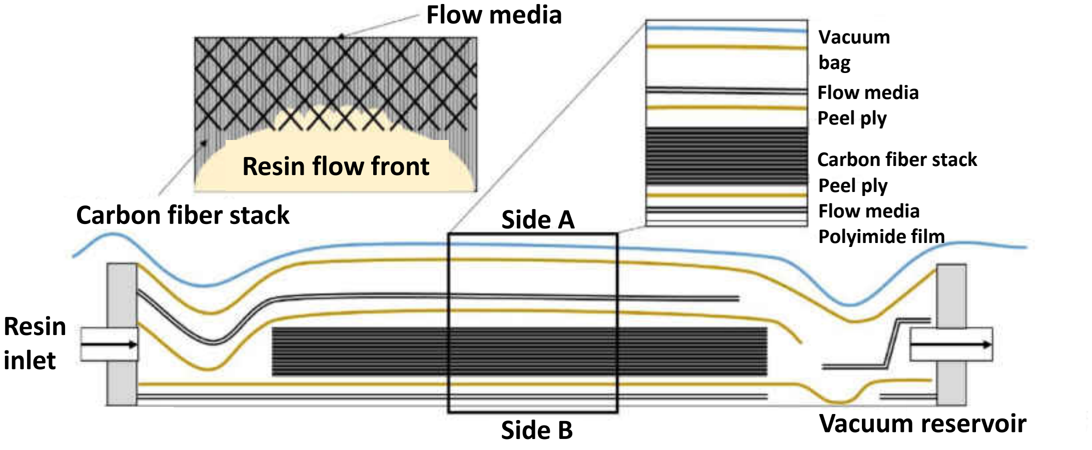

Figure 4.1: Schematic of resin infusion under flexible tooling (RIFT) method

Three particle loadings, 6 wt%, 9 wt% and 12 wt% with RSCA, NRSCA or untreated surface nanoparticles are studied in this work. Two samples from each of nine categories were tested providing a total of 18 samples. Each set was cut from different locations from the same composite sheet using a waterjet cutter. The fiber volume fractions of the composites were measured for validation using optical microscopy of cross-sections. Carbon fiber volume fractions of $57 \pm 3\%$ were obtained for the finished composites.

Sample Preparation

Here, we describe the details of the sample preparation. Upon curing, samples were machined from the bulk composite material for analysis. Waterjet cutting was utilized due to the techniques low cutting force and lack of thermal distortion, which is associated with other machining techniques [84]. The sample dimensions were selected as 100x10x3 mm^3. A sample along with a schematic are presented in Figure 4.2. The sample surface is seen to not be completely smooth and instead is patterned with regularly spaced hills and troughs. This patterning is the artifact of the flow media used during infusion of resin which is shown in Figure 4.1.

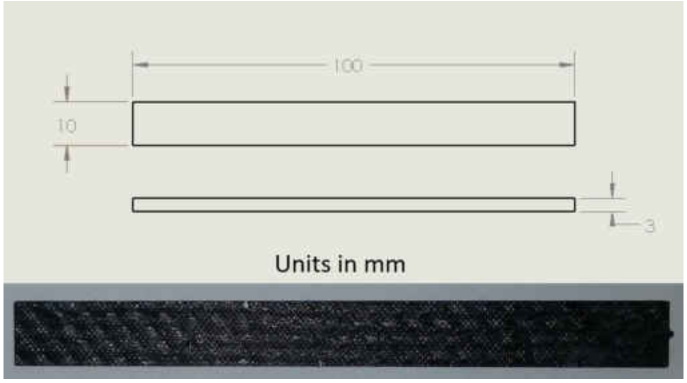

Figure 4.2: Schematic of design with labeled dimensions and image of a sample before test

Experimental Setup

The experiment was carried out in two phases; in the first phase, dispersion of the alumina particles at both sides of the sample were determined using the portable piezospectroscopy system. These dispersion maps not only produces results for dispersion and sedimentation analysis, but also allows for the identification of each side, side A and side B, of the sample. Side A was noted to identify lower alumina content while side B contains more alumina contents due to sedimentation effect. The piezospectroscopic data was collected on side B that held large amount of particles whereas DIC images were taken from side A. In the second phase, unidirectional tensile test was performed on the samples and piezospectroscopic and digital image correlation (DIC) data were collected simultaneously with the increased load.

Portable Piezospectroscopy System

The main system used for the non-contact stress measurement experiments is a novel and compact system named the Portable Piezospectroscopy System [4]. This system utilizes a spectrograph, a charge-coupled device (CCD), as well as a laser source and X-Y-Z stages, providing mapping capabilities, as can be seen in Figure 4.3. Additionally, this portable system has a computer used for data collection and deconvolution is carried out using software for the deconvolution and fitting. [4].

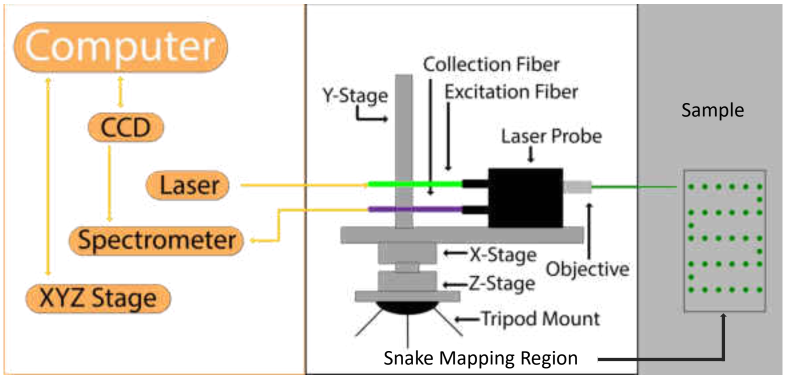

Figure 4.3: Portable piezospectroscopy system is used to take snake scans of the samples. LightField^{TM}and COSMOS^{TM}are used with CCD and XYZ stage to organize maps sizes and settings.[4]

Experimental Parameters and Procedure

At the first phase of the experiment, photoluminescence measurement of 12x22 mm^2 area on each side of the samples was collected. A diode-pumped solid-state (DPSS) laser of 532nm wavelength with maximum 300 mW output power was used in the portable piezospectroscopy system (PPS) [4] to collect data at spatial resolution of 500 microns. Laser power was varied from 20 mW to 50 mW and collection time was adjusted optimizing intensity and noise from signal. A cooling tube from an air compressor was used to mitigate any heating possibility due to laser emission. Dispersion maps for each side was plotted as Figure 5.1 to identify side A and side B. Side A was chosen for DIC speckling while higher alumina particles quantity on side B were expected to provide higher intensities for higher quality piezospectroscopic data during loading.

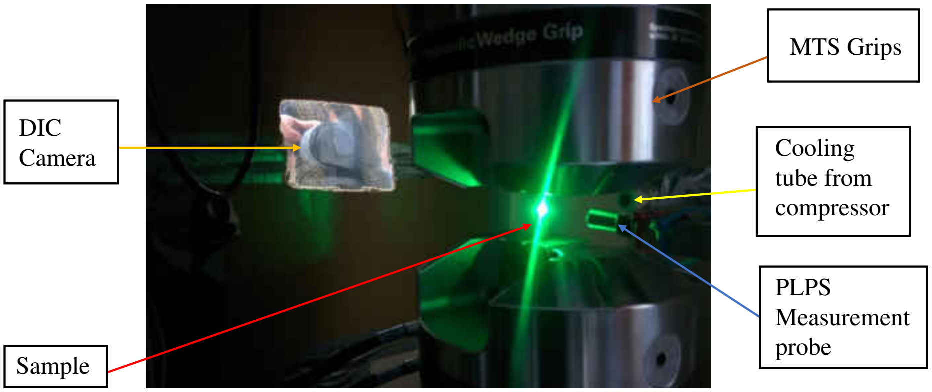

Figure 4.4: Experimental setup for uniaxial tension test with piezospectroscopy and DIC camera

A servohydraulic MTS universal testing machine fitted with serrated grips was used for uniaxial tensile test using medium graded emery cloth between the grips and the sample [85]. Displacement control is used with cross-head speed of 0.5mm/min and a limit of 20 kN axial load. At each 5kN load increment, the sample was held at a constant displacement and PS data was collected. The hold time for each sample is varied from two to eight minutes depending on the collection time for PS map. DIC data was collected continuously during the experiment. Figure 4.4 shows the experiment setup.

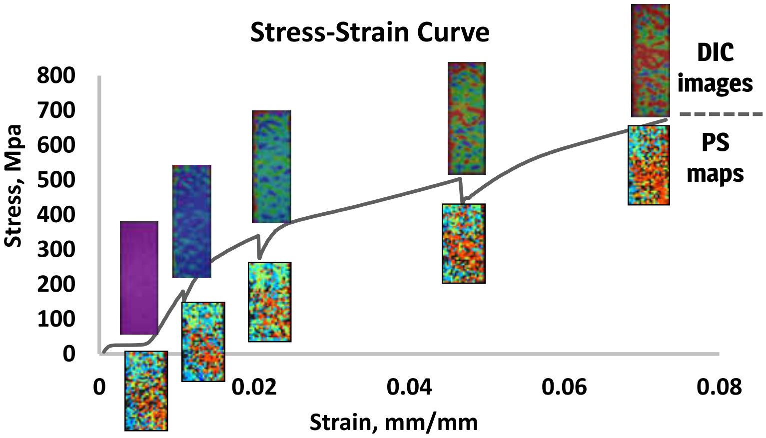

Figure 4.5: Piezospectroscopic and DIC data collection with increased tensile load

During the holds at each 5 kN increment, the material experienced a drop in stress as a result of stress relaxation. The highest drop in stress was recorded as 50 MPa for which shift in R1 peak was not significant. Also, as displacement control was used for the tensile loading, DIC images were consistent before and after the stress relaxation.

To reduce the effect of laser power on the samples, a simple test was performed using the temperature effect on the characteristic R-line of the alumina nanoparticles. Previous work has indicated that the peak positions of the R-lines tend to shift toward smaller wavenumbers as temperature is increased [86, 87]. Temperature effect on epoxy-alumina nanocomposite with 5 vol% alumina nanoparticle is shown as in Figure 4.6 [5]. The temperature coefficient found in this study was -0.098 $cm^{-1}/°C$.

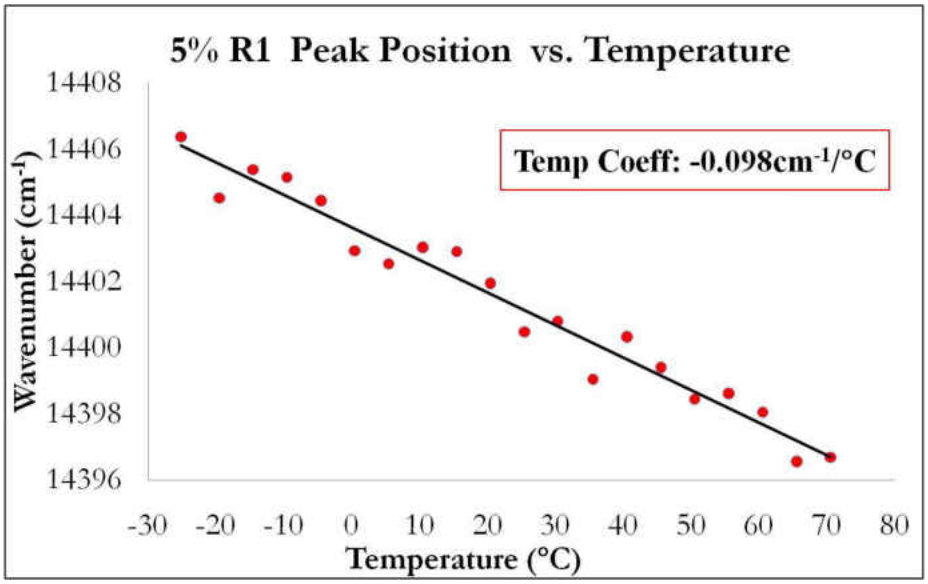

Figure 4.6: Temperature effect on R1 peak position for 5 vol% epoxy-alumina nanocomposite [5]

For determining the effect of laser power in increasing temperature or damaging the sample, laser was pointed at one spot on a sample for 30 to 60 seconds with varying laser power and spectroscopy data was collected. Figure 4.7 shows variation in R1 peak position with time.

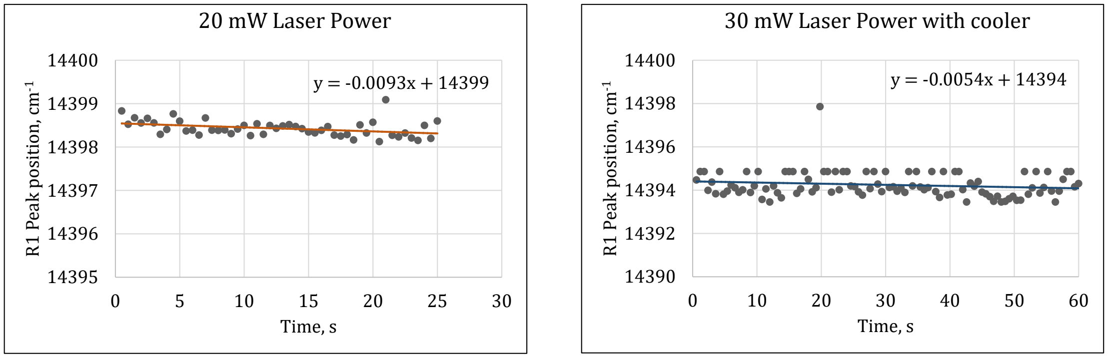

Figure 4.7: Temperature effect on R1 peak position for HCFRP sample without and with cooling system

In Figure 4.7, the plot for 20 mW laser power is showing a negative slope with increasing time which is almost one-hundredths of what found for epoxy-alumina nanocomposite. To make sure that no damage or increase in temperature is occurring during the test, compressed air flow is used and spectroscopy data with 30 mW laser power was collected. The plot for 30 mW laser power in Figure 4.7 shows a drop in negative slope even for higher focusing time and laser power. In actual experiment, the laser was focused at one point not more than 800 ms. Thus, the cooling system is found effective for this experiment.

CHAPTER 5: PIEZOSPECTROSCOPIC STUDY OF HCFRP WITH SIMULTANEOUS DIGITAL IMAGE CORRELATION (DIC)

Objectives

Implementing the methods described in Chapter 2, dispersion maps and piezospectroscopic maps are plotted for each weight percentage and surface treatment with varying applied tensile load. Side-by-side plots of dispersion, piezospectroscopy and DIC are then compared and analyzed to determine correlation between the weight percentages, surface treatments and characteristic of the nanoparticles in the material while it experiences mechanical load. In each case, these variables and their effect on dispersion, residual stress and stress due to loading are discussed. Comparisons are made with the theoretical approach of rule of hybrid mixtures.

Photoluminescence spectroscopy, piezospectroscopy and DIC results from HCFRP Samples

Figure 5.1 shows the intensity maps or representative dispersion for each side of the sample for all three weight percentages and treatment conditions. Overall results from a total of nine combinations of samples are presented in Figure 5.2 -5.10. Each figure shows the dispersion in the first row obtained from intensity, piezospectroscopic maps in the second row from peakshifts and the DIC maps in the third row for different loads. The unit of the intensity in dispersion maps are arbitrary. The numeric value of the highest intensity varies from sample to sample depending on weight percentage and sedimentation of alumina nanoparticles. The numeric value of the limits of piezospectroscopic maps also vary sample to sample and the range depends on the stress state of the alumina nanoparticles. These maps represent the stress within only the nanoparticles in terms of their spectral shifts. At zero applied load, the maps show the residual stress from manufacturing.

All the DIC maps have the same scale as the strain is measured globally and it is independent of intrinsic parameters that are typical in piezospectroscopic measurement. While the PS maps provide the information on the nanoparticles' stresses at the microscale only due to the applied load, the DIC maps show global strain as the load is increased.

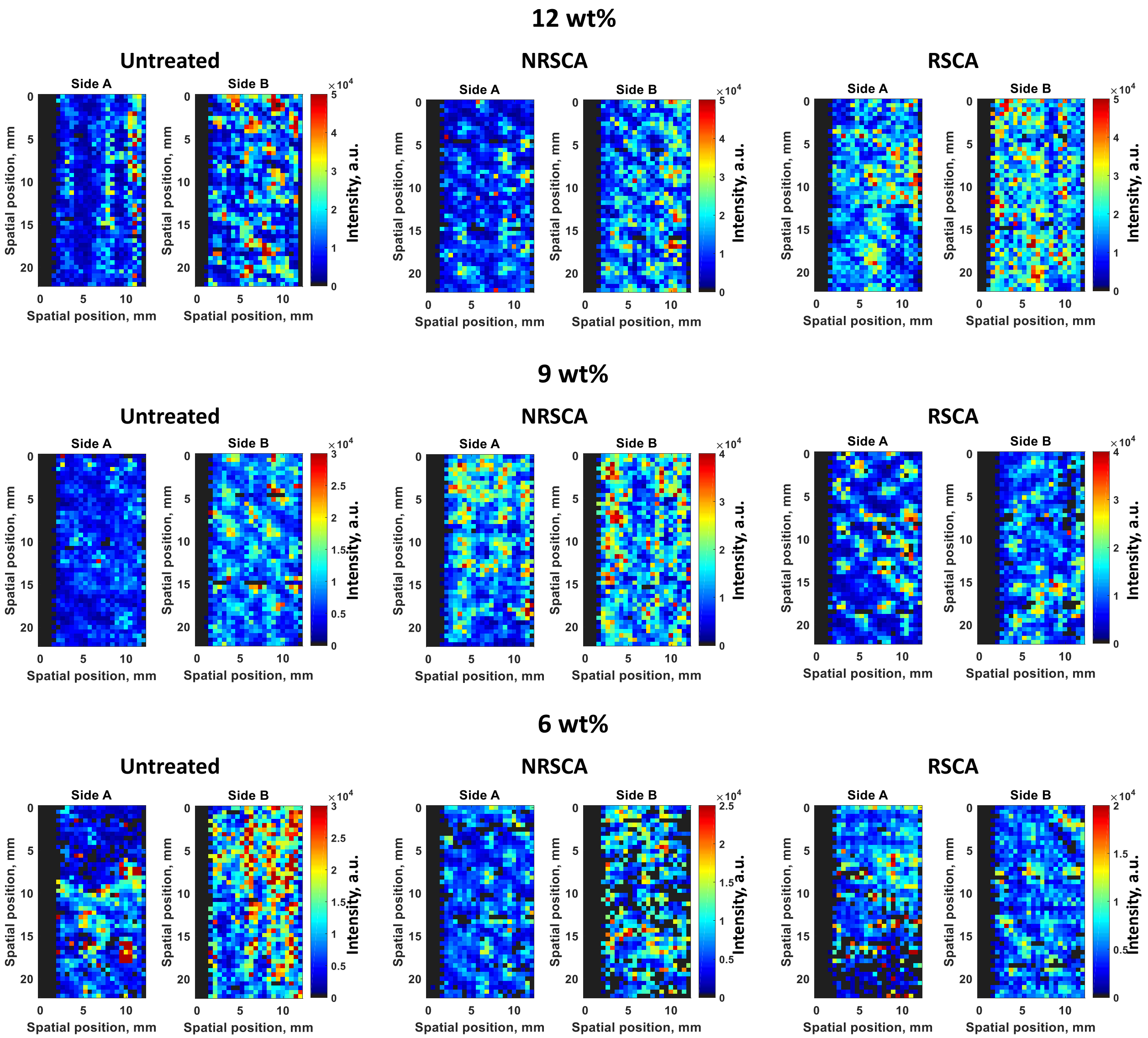

Figure 5.1: Dispersion maps for both sides of each combination of samples

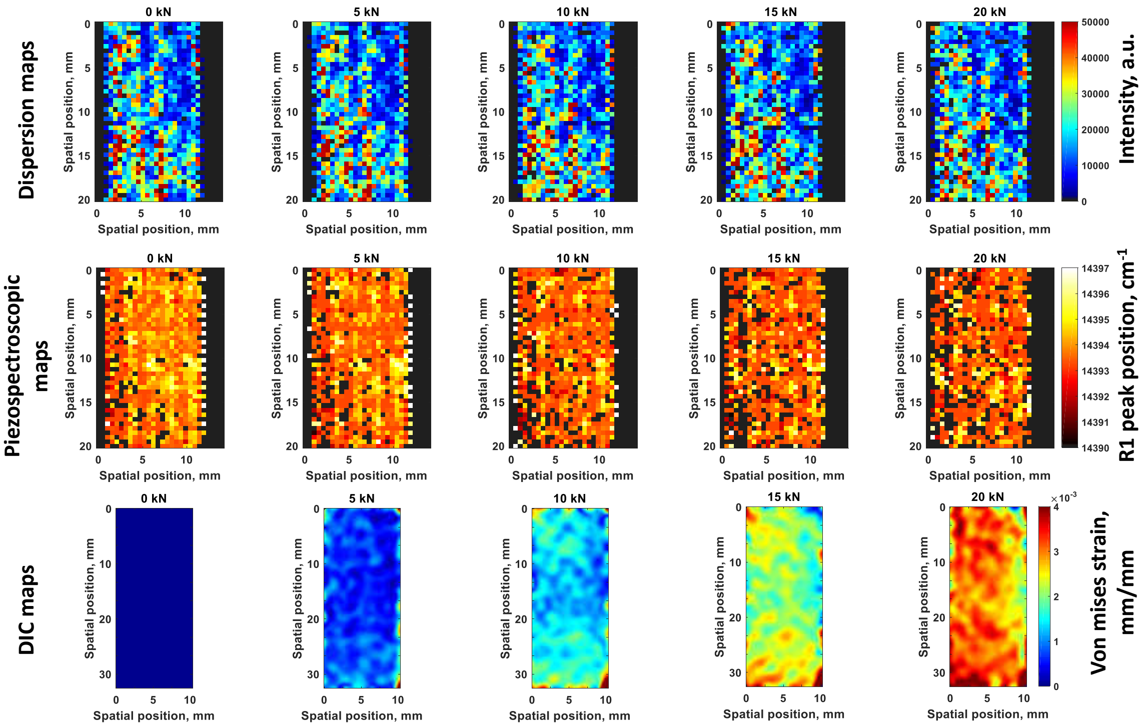

Figure 5.2: Dispersion maps, piezospectroscopic maps and DIC maps for **untreated 6 wt%** alumina HCFRP sample

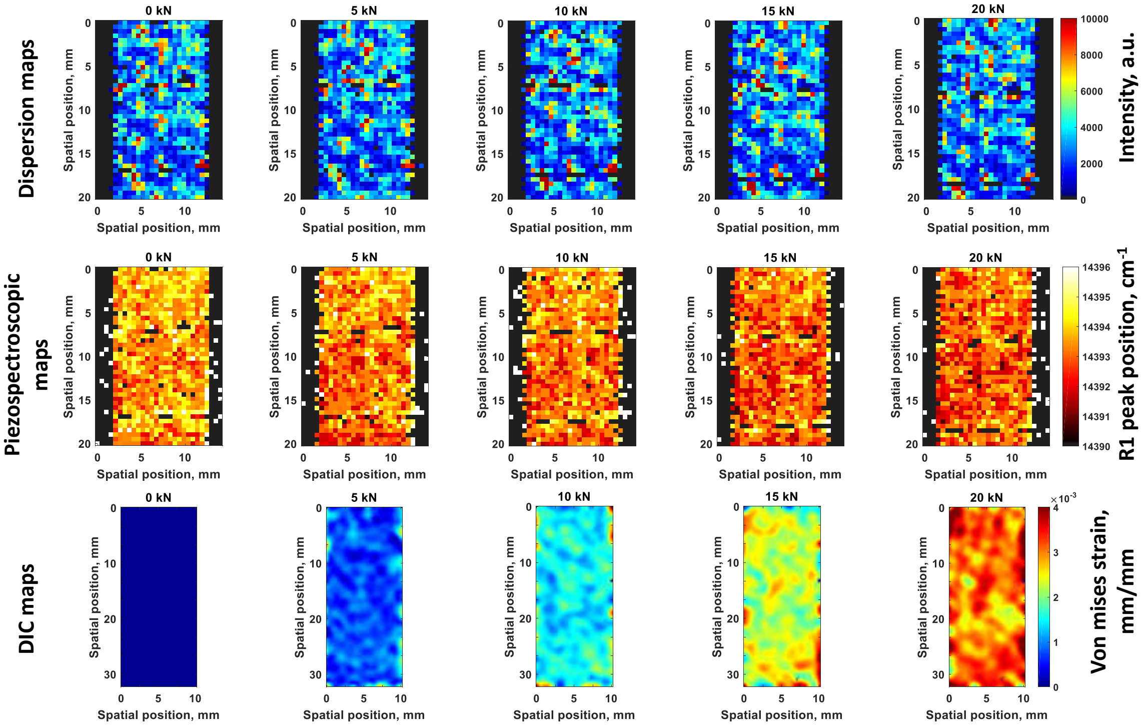

Figure 5.3: Dispersion maps, piezospectroscopic maps and DIC maps for **NRSCA treated 6 wt%** alumina HCFRP sample

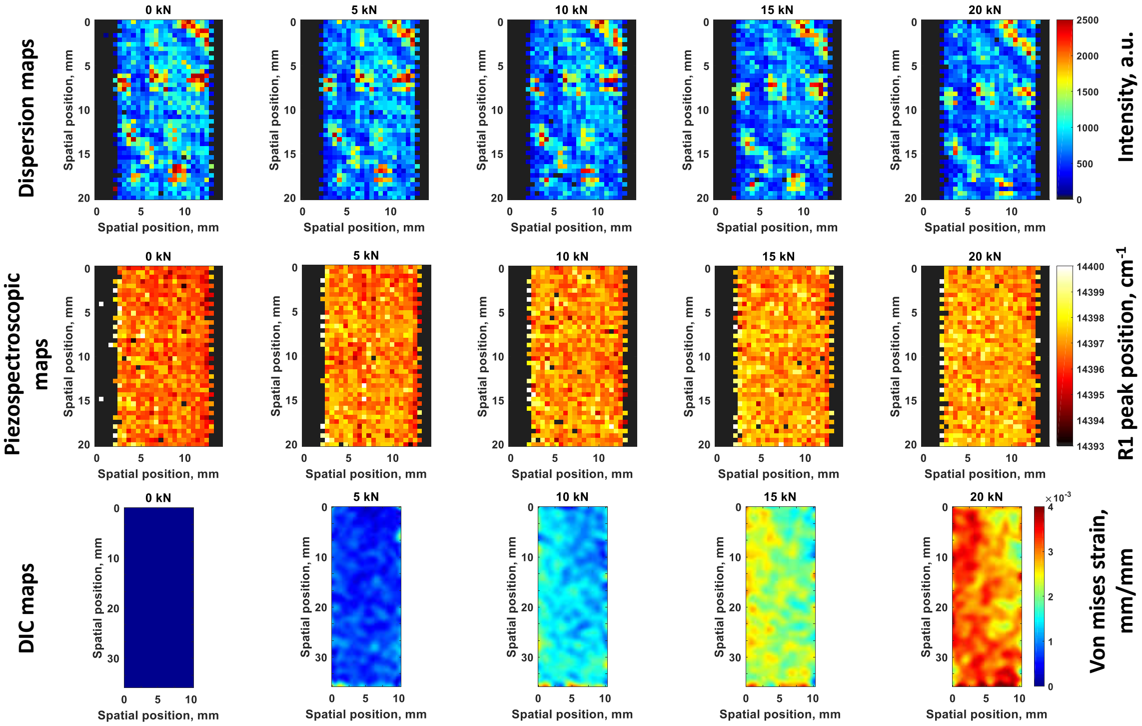

Figure 5.4: Dispersion maps, piezospectroscopic maps and DIC maps for **RSCA treated 6 wt%** alumina HCFRP sample

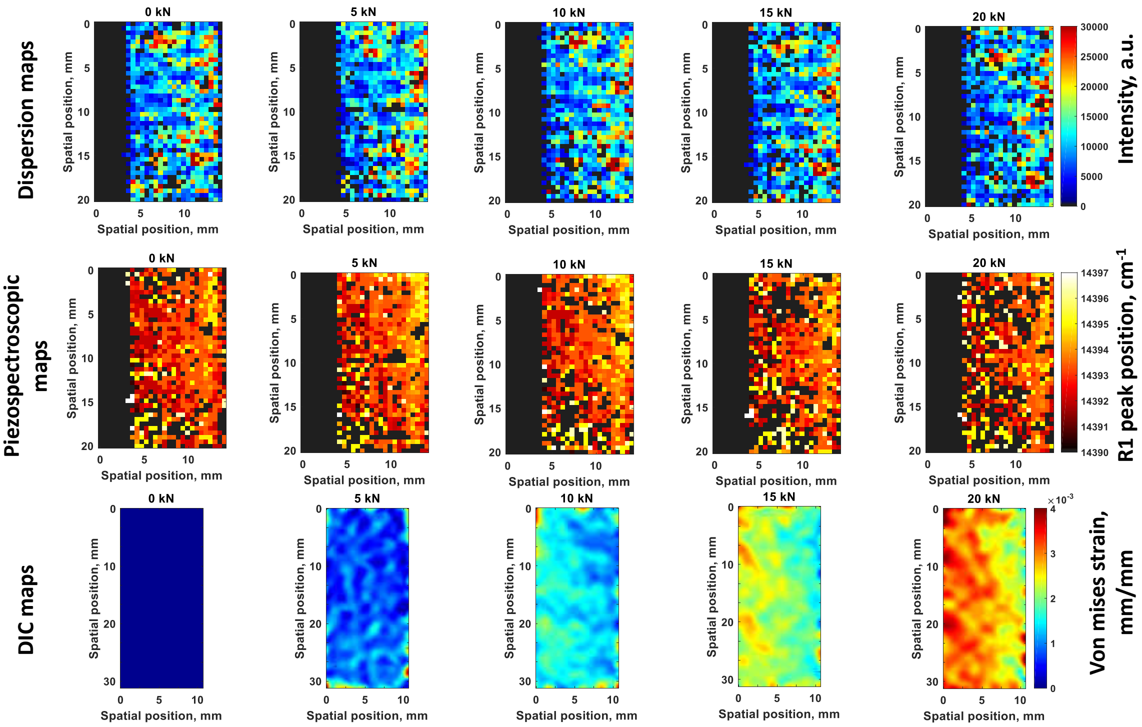

Figure 5.5: Dispersion maps, piezospectroscopic maps and DIC maps for **untreated 9 wt%** alumina HCFRP sample

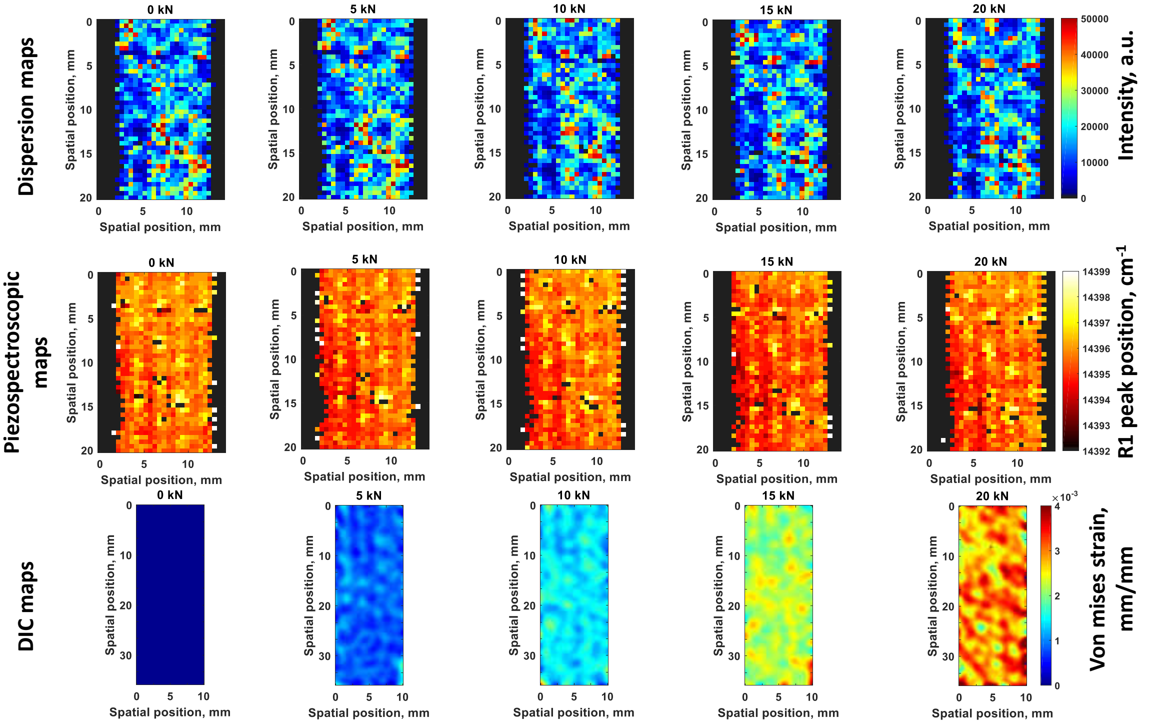

Figure 5.6: Dispersion maps, piezospectroscopic maps and DIC maps for **NRSCA treated 9 wt%** alumina HCFRP sample

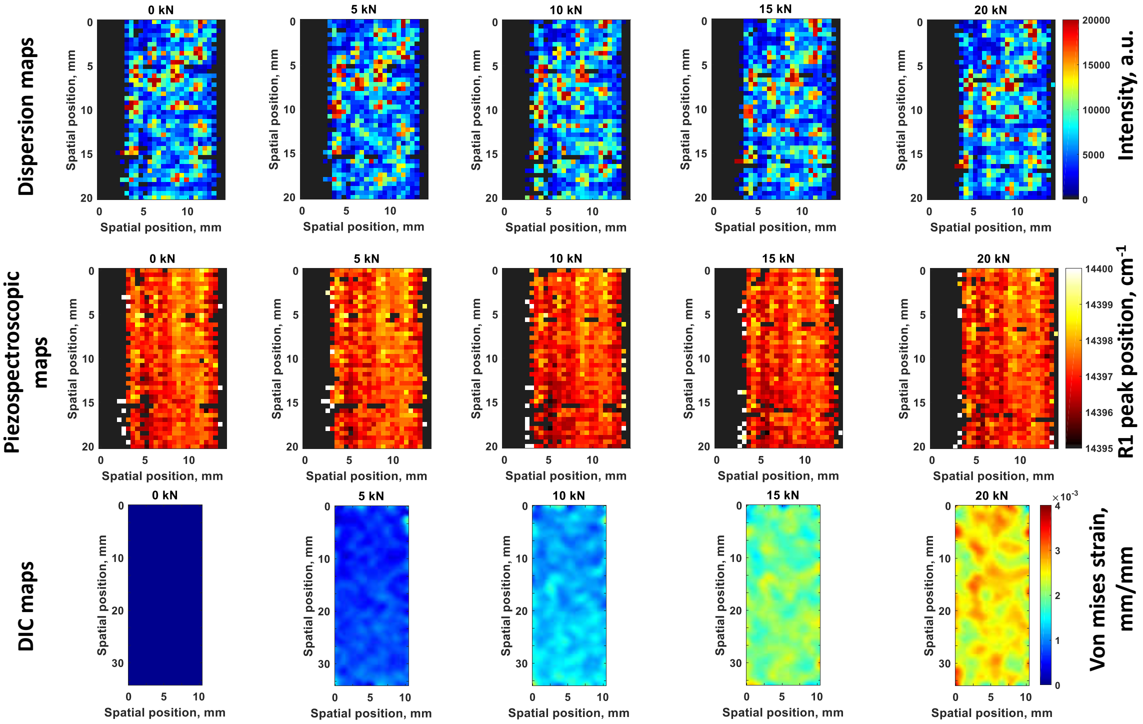

Figure 5.7: Dispersion maps, piezospectroscopic maps and DIC maps for **RSCA treated 9 wt%** alumina HCFRP sample

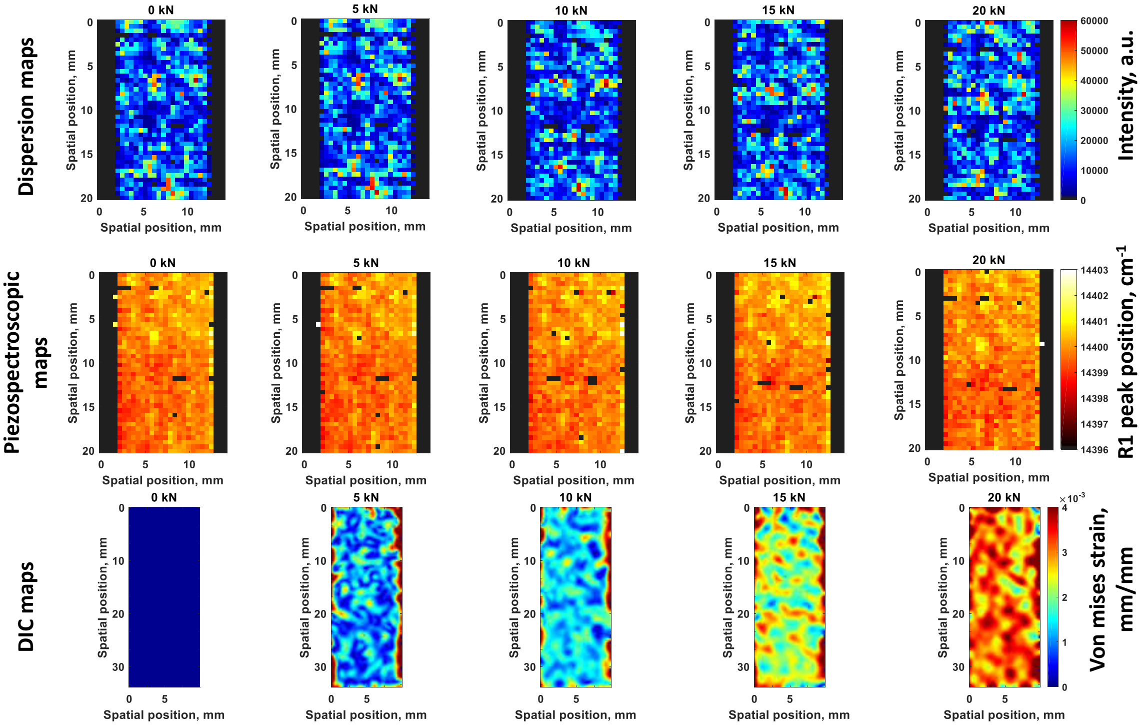

Figure 5.8: Dispersion maps, piezospectroscopic maps and DIC maps for **untreated 12 wt%** alumina HCFRP sample

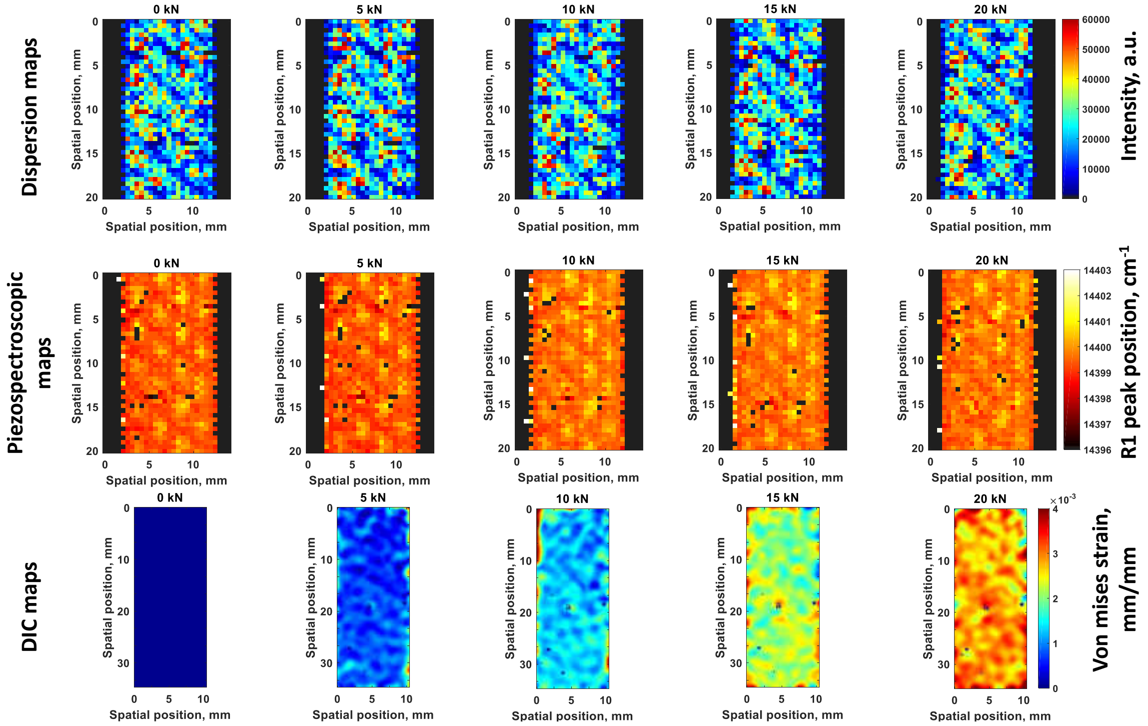

Figure 5.9: Dispersion maps, piezospectroscopic maps and DIC maps for **NRSCA treated 12 wt%** alumina HCFRP sample

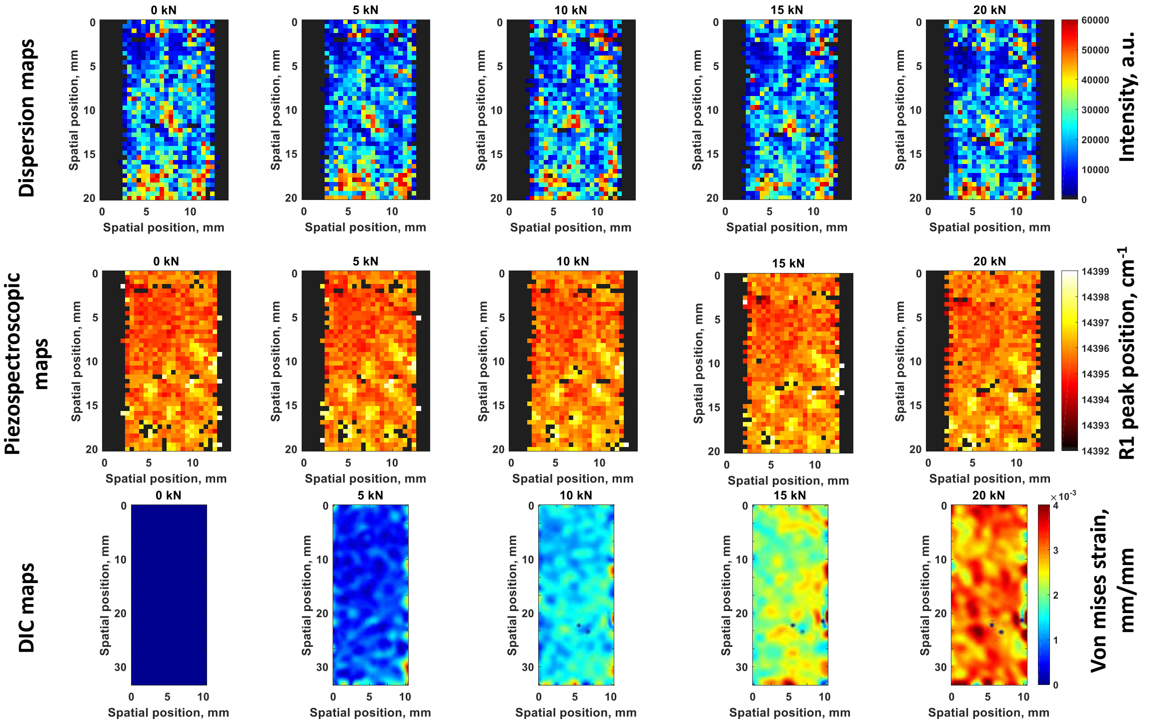

Figure 5.10: Dispersion maps, piezospectroscopic maps and DIC maps for **RSCA treated 12 wt%** alumina HCFRP sample

Dispersion of Nanoparticles

Variation in Dispersion due to Weight Percentage

Figure 5.1 highlights that the samples with untreated particles tend to provide the largest amount of agglomerations and sedimentations among all weight percentages, except in the 9 wt% sample.

This is seen through the large intensity variations between the surfaces in the 12 wt% and 6 wt% samples. The 9 wt% sample has the best dispersion of particles for the untreated set in terms of less sedimented particles and less agglomeration. The samples also exhibit low concentration lines which run diagonally in both directions as shown in Figure 5.11. The figure shows the concentration lines on the dispersion maps of 12 wt% NRSCA treated sample.

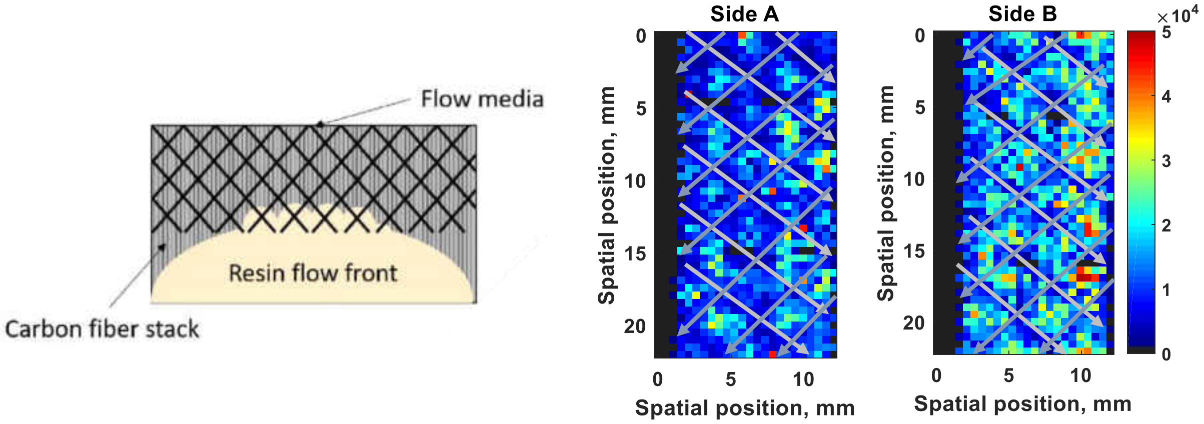

Figure 5.11: Low conecentration lines as a result of flow media pattern during manufacturing marked on the dispersion map

These low concentration lines are also observed in the surface treated samples and are artefacts of the manufacturing process. They share the same pattern as the distribution media used in the RIFT process; and as such, locations where the fibers of the distribution medium impinged on the sample show lower concentrations of particles due to a reduced thickness of resin on the surface of the fiber composites. This effect seems to be reduced by the presence of surface treatments, future work will consider testing the effects of distribution media during manufacturing in order to improve the dispersion of the particles.

Variation in Dispersion due to Surface Treatment

Comparing the dispersion maps of treated and untreated particles for all the weight percentages in Figure 5.1 it is observed that, in general the dispersion of particles is improved with the application of surface treatments. The amount of agglomerated particles is also reduced with the application of surface treatments. In both samples with treated particles, the 12 wt% samples have the least homogeneous dispersion of particles and the 6 wt% samples have the most homogeneous dispersion of particles. Between both surface treatments, it is seen that the RSCA treatment tends to provide for smaller intensity gradients indicating better dispersion. The same pattern on the surface of the composites due to the imprint of the fibers of the infusion mesh through the peel ply, is present in both treated samples. Differences in the amount alumina nanoparticles present on the surfaces reduces the homogeneity of the material which will further affect the mechanical properties of the material. The measurement of intensity obtained in this work highlights inhomogenity and can be used to establish effects of preventive approach during manufacturing.

Residual Stress of Alumina Nanoparticle

Residual stress is defined as a stress that persists free of external forces or temperature gradients [88]. In composite systems this occurs when one component limits the strain of another [89], through differences in material properties such as coefficient of thermal expansions or elastic modulus. In reinforced polymer composite systems, the primary source of residual stress is due to volumetric shrinkage associated with the polymerization reaction of the matrix [90]. These stresses occur as a result of a conversion of the matrix from a viscous-plastic phase to a rigid-elastic phase [91]. This conversion is accomplished through covalent bonding of monomers for the development of a polymer network. The bonding decreases distance between the separate groups of atoms, resulting in decreased atomic spacing and decreases in overall volume. The incorporation of fibers and nanoparticles that do not accommodate this shrinkage results in residual stresses characteristic of composite materials. Applied surface treatments have an effect on the bonding of the particle to the matrix, effectively adjusting the properties of the interphase [92, 93, 94]. This is expected to result in differing residual stress states on particles with different surface treatments. The residual stress in the material can impact the mechanical properties and hence the measurements of these stresses are of significance in nanoparticles.

Residual Stress due to Different Surface Treatment/Dispersion

The first map of piezospectroscopic maps in the second row from Figure 5.2 to Figure 5.8 shows the peak shift corresponding to the residual stress of the alumina nanoparticles, as the stress of the nanoparticles has a direct relation to the R1 peak position as per the Equation 2.2. As the R1 peak position at 14402.3 cm^{-1} is known to be in the unstrained state [95], any value lower than that expresses compressed state of the particles as per the piezospectroscopic characteristic of alumina. Observing the first piezospectroscopic map in the figures and comparing them with the dispersion maps, it can be stated that, the locations with less alumina particles are in a more compressive state than the particles which are sedimented. Figure 5.12 shows how the particles are visible on the sedimented surface on one side of the sample. Also, due to the flow media pattern, low concentration lines show more compressive stress on the surface.

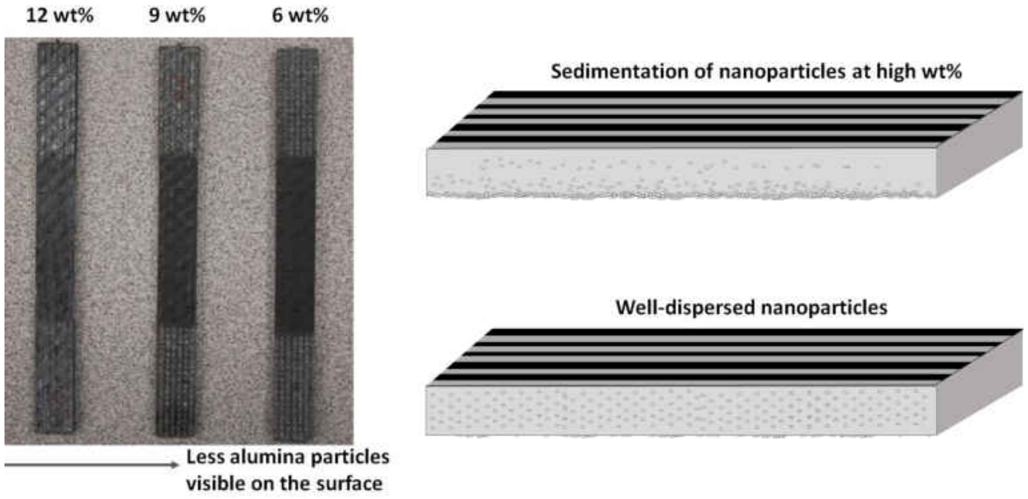

Figure 5.12: Untreated 12 wt%, 9 wt% and 6 wt% samples show the visibility difference of the alumina nanoparticles on the surface due to sedimentation and wt%

To compare the residual stress on the particles for different surface treatment, average R1 peak position of the particles are calculated and plotted as Figure 5.13. The plot shows consistency in residual stress of RSCA treated particles that is less compressive for all the weight percentages. It is expected that the RSCA treatment helps the particles to be well dispersed in the material thus reducing contact among the particles. This phenomena likely reduces the residual compressive stress in the RSCA treated particles as observed in Figure 5.13.

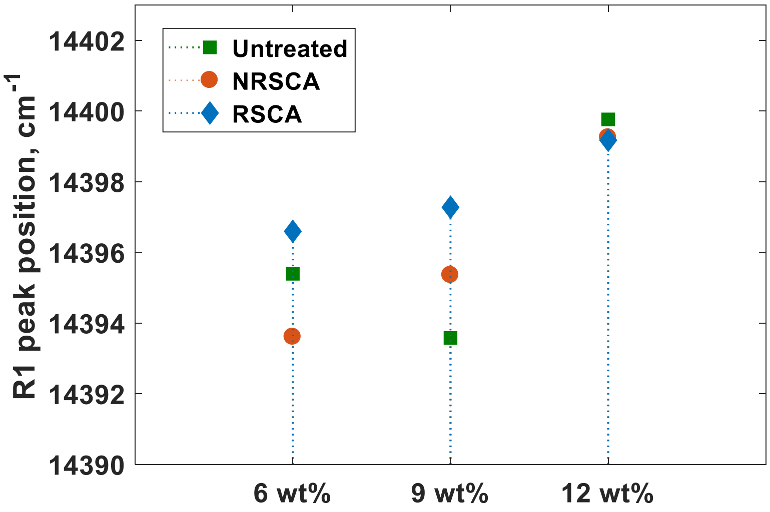

Figure 5.13: Residual stress on particles for all the combinations

In the dispersion maps shown in Figure 5.1, for 12 wt% samples, we see that the sample with untreated particles experiences slightly more sedimentation than the treated ones. Thus, the untreated particles are slightly less compressive than the treated particles for the 12 wt% samples. As the particles are highly sedimented, the compressive stress due to particle contact dominates and this will be discussed later. Overall the 12 wt% samples has less compressive residual stress as it is heavily sedimented and most of the particles lie on the surface. In 9 wt% samples, surface treatment dominates the residual stress behavior of the particles. RSCA treatment strongly reduces agglomeration of the nanoparticles and the particles have less contact stress whereas untreated particles show high compressive stress. For 6 wt% samples, sedimentation of the particles are dominating the contact stress of the particles having less compressive stress than NRSCA treated particles.

Effects on Residual Stress due to Loading

The piezospectroscopic maps in the second row of Figure 5.2 to Figure 5.10 shows the variation of the stress on the nanoparticles due to the applied tensile load on the samples. It was expected to observe upshift of the R1 peak position i.e. increasing the peak position due to an expected increase in tensile stress on the particles with increasing tensile load. However, 6 wt% untreated and NRSCA treated particles, 9 wt% NRSCA treated particles and 12 wt% RSCA, NRSCA and untreated particles show the opposite characteristic. Treatment with RSCA ensures strong bond of particles with the resin and particles that are well-dispersed in the material. Thus, when the sample is loaded with tensile load, alumina nanoparticles contributes accordingly to the load. The piezospectroscopic maps for RSCA treated alumina samples for almost all weight percentages show the upshift in R1 peak position though the amount of change in the upshift decreases with increased particle weight percentage.

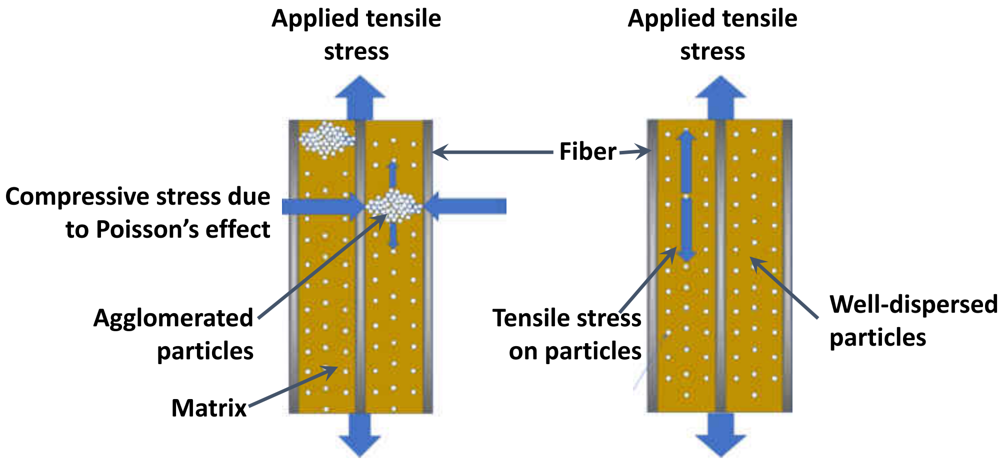

Figure 5.14: Tensile stress effect on agglomerated and well-dispersed particles

NRSCA and untreated alumina nanoparticles show a downshift i.e. decrease in R1 peak position with increasing tensile stress. From earlier residual stress comparison, these samples already have high compressive residual stress due to their particle contact stress. With increasing tensile load, it is observed that the agglomerated nanoparticles are experiencing more compressive stress instead of sensing tensile stress.

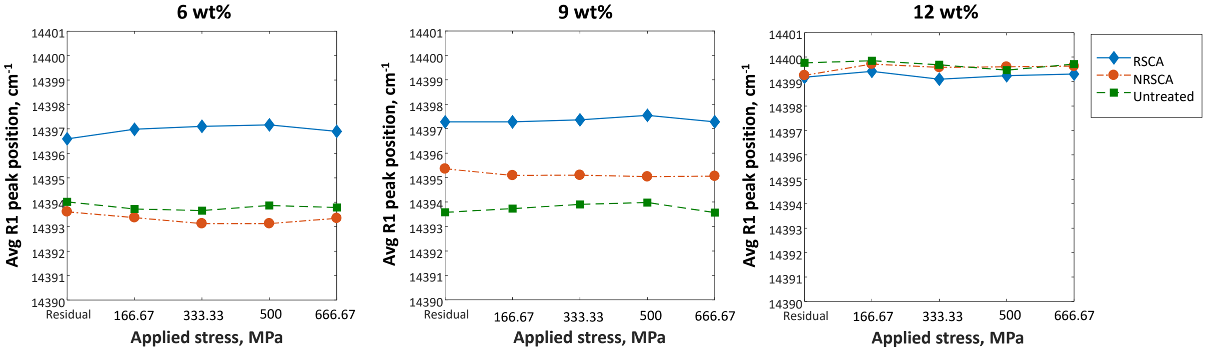

Figure 5.15: Varying stress on alumina nanoparticles due to applied stress on the samples for different particle weight percentages

To compare the stresses on the nanoparticles for different samples, the average R1 peak position for a sample is plotted for different applied stress in Figure 5.15. For 6, 9 and 12 wt% RSCA treated particles, change in R1 peak position due to applied tensile stress follow a slight upshift as also observed in the piezospectroscopic maps. However, this change is too small to quantify a trend. From the plot, variation in peak shifts for different weight percentages can be compared. As 12 wt% samples have highest particle concentration, variation between the treated and untreated particle behavior is negligible compared to the other weight percentages' functionalization. Insensitivity of particle stress to the overall applied stress to the composite is the general observation here and in order to investigate this further, the theoretical approach of rule of hybrid mixture (RoHM) was used.

Rule of Hybrid Mixtures

To determine the strength of a composite material that consists of two different modulus material, rule of mixtures is a well-known approach [96, 97, 98]. An extended version of the method to use for three-material composite is

$$E_M = V_f E_f + V_m E_m + V_a E_a \tag{5.1}$$

where subscripts M, f, m and a stand for the material, fiber, matrix and alumina nanoparticles respectively, E is the Modulus of Elasticity and V is the volume percentage [99]. From the equation of RoHM, it is possible to estimate the amount of stress taken by the alumina nanoparticle. Figure 5.16 shows the particle stress in both RoHM and piezospectroscopic method for each combination. Note that the stress in the particle for piezospectroscopic mrethod uses the Equation 2.2 and is based on the averaged peakshift over the measured area.

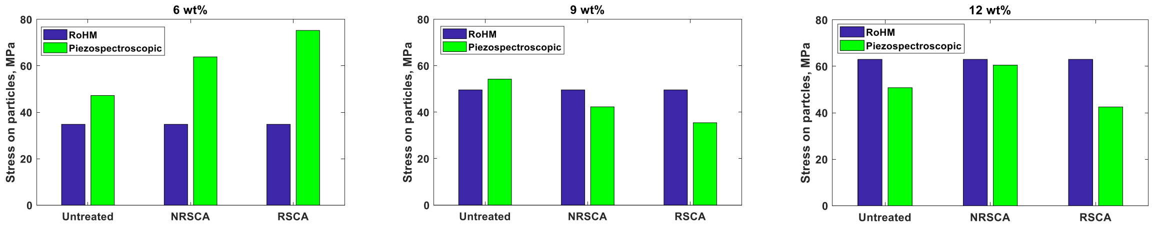

Figure 5.16: Contribution to applied stress (666.67 MPa) using RoHM and piezospectroscopic method from alumina particles

In general, both RoHM and PS values for stress fall in the same order of magnitude. This validates PS capability to obtain stress in alumina. As the equation of RoHM does not consider the surface treatment but includes the volume percentage, RoHM value of stress for same weight percentage is the same for each functionalization. Whereas piezospectroscopic stress shows difference in stress on particles due to different surface treatments. From 6 wt% alumina particles, stress contribution by the particles are higher than that estimated using RoHM method and the highest amount of load is carried by the RSCA treated particles which is almost double of RoHM estimates confirming that functionalization plays a significant role in load transfer for 6 wt%. As the weight percentage of alumina particles increases, RSCA treated particles contribute less to load sharing. It is hypothesized that the less load on the particles means less debonding and damage which makes the material quality better. Although we would like the particles to take more load for sensing, this counteracts its role to improve mechanical properties.

Third rows of Figure 5.2 to Figure 5.10 present the DIC results with applied uniaxial load and show the global strain of the material whereas the second rows show the stress on the particles only. The strain maps also show the flow media pattern which conforms to the different stress region of the material observed in the piezospectroscopic maps. Comparing the DIC maps with the dispersion maps of side A in Figure 5.1, certain differences in the strain regions can be identified. It is observed that the regions with agglomerated particles are having lower strain rate. In the discussion of piezospectroscopic maps, it was seen that the agglomerated particles are having negligible stress state. Thus, where DIC data only shows the mechanical response of the whole material, piezospectroscopic maps show the particle stress individually and can also be related to the strain.

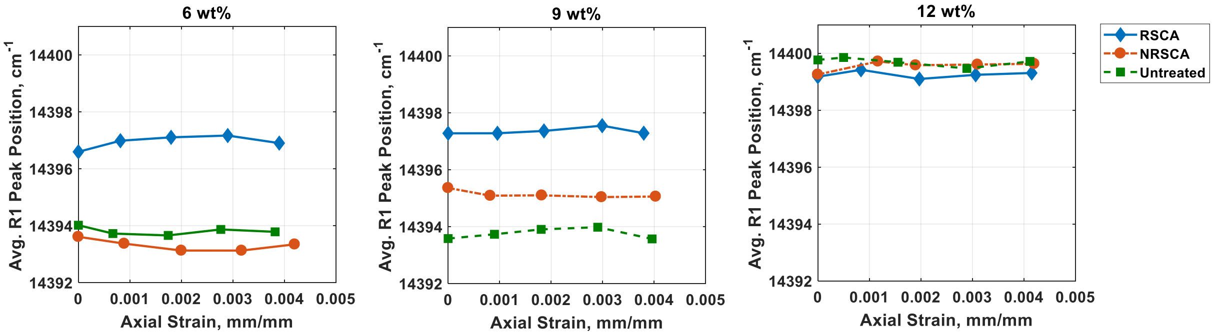

Figure 5.17: Varying strain on alumina nanoparticles due to applied stress on the samples for different particle weight percentages

Plots in Figure 5.17 show the relation between average R1 peak position representing stress on the nanoparticles and axial strain measured from DIC. The plots corroborate the results found in Figure 5.15 as a fact that the applied uniaxial tensile stress caused global strain in different strain rates. The strain rate for the same amount of applied stress is varying for different of the samples. Though the applied uniaxial tensile stress was not continuous, a stress-strain curve can be still plotted for each load before hold as shown in Figure 5.18.

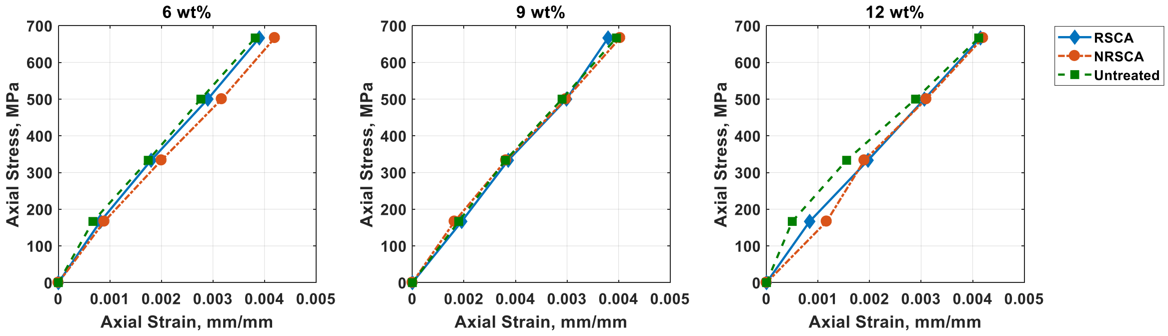

Figure 5.18: Stress-strain curve for HCFRP samples

The stress-strain curve in Figure 5.18 is plotted for applied stress and resulting global strain measured from the DIC system for all the samples tested. From the dispersion analysis, 6 wt% showed improvement in particle dispersion with surface treatment. The stress-strain curve for 6 wt% samples are showing improved toughness for RSCA and NRSCA treated particle embedded samples. For 9 wt% samples, the stress-strain curve coincides with each other as the samples have consistency in dispersion characteristics throughout all the surface treatments. All the samples from 12 wt%, have non-linear mechanical properties and from previous dispersion results, it was observed that the samples have more agglomeration and sedimentation of the alumina nanoparticles. Thus, it is clear from the stress-strain curves and dispersion analysis that, dispersion characteristics have direct effect on the overall mechanical performance of the material.

Novel Conclusions

In this chapter, results obtained from dispersion maps, piezospectroscopic maps and DIC maps are analyzed and compared to identify particle behavior under applied load. Dispersion map of each side of the samples shows the sedimentation properties for different surface treatment and weight percentage of alumina nanoparticles. Among untreated particles, 9 wt% sample is found to have best material properties in terms of dispersion and sedimentation. NRSCA and RSCA surface treatment improved the dispersion and reduced the sedimentation and agglomeration for each weight percentage.

Residual stress of the particles inside the material was identified using piezospectroscopic maps at zero load. Difference in residual stress depends not only on the surface treatment and weight percentage, it also dependent on particle agglomeration and sedimentation, i.e. manufacturing quality.

Mechanical response of the alumina nanoparticles was also possible to determine using piezospectroscopic characteristic of the alumina particles. It concludes how the homogeneous dispersion and less agglomeration contribute to sensing the applied stress.

Theoretical approach using rule of hybrid mixtures was performed and compared to the piezospectroscopic result which shows that the RoHM method can estimate the particle stress whereas piezospectroscopy can determine actual stress acting on the embedded particles. The DIC maps also conforms to the stress states on the materials due to agglomeration and sedimentation. Global stress-strain curve shows relation to the dispersion quality of the samples.

CHAPTER 6: CONCLUSIONS AND FUTURE OUTLOOK

In this work, manufacturing parameter effects on particle dispersion and mechanical response are investigated through photoluminescence piezospectroscopy with concurrent digital image correlation measurements. From the dispersion maps it was found that the application of silane coupling agents to the nanoparticles provided for improved dispersion.

Furthermore, the surface treatments tend to provide for more consistent dispersion regardless of weight percentage. Future work will consider different manufacturing process to reduce the agglomeration and low concentration lines caused by the flow media in the RIFT process.

The residual stress analysis shows the difference in residual stress of the particles that are sedimented, agglomerated or well-dispersed inside the material. Dispersion of the particles and the surface treatment and weight percentage play a vital role in residual stress of the particles as the dispersion of the particles is dependent on this parameters.

DIC was used to relate global strain behavior to the micro-level stress of the embedded particles. With the use of photoluminescence piezospectroscopy, it was possible to identify the stress acting on the particles individually. As the load contribution from the nanoparticles was small compared to the applied load on the material, embedded nanoparticles are effective in improving material properties such as wear resistance, fracture toughness rather than acting as a stress-sensor in the current configuration.

Previous research shows high stress-sensitivity of nanoparticles when it is applied as a coating on the surface. Future work will consider a layer of nanoparticle coating which may act as a stress-sensor. In this work, particle size was not varied. Variation in particle size may provide more stress-sensitivity maintaining the desired material quality.

LIST OF REFERENCES

[1] A. Stevenson, A. Jones, and S. Raghavan, “Characterization of particle dispersion and volume fraction in alumina-filled epoxy nanocomposites using photo-stimulated luminescence spectroscopy,” *Polymer Journal*, vol. 43, no. 11, pp. 923–929, 2011.

[2] I. Hanhan, A. Selimov, D. Carolan, A. C. Taylor, and S. Raghavan, “Quantifying alumina nanoparticle dispersion in hybrid carbon fiber composites using photoluminescent spectroscopy,” *Applied Spectroscopy*, vol. 71, no. 2, pp. 258–266, 2017.

[3] A. Manero II, A. Selimov, Q. Fouliard, K. Knipe, J. Wischek, C. Meid, A. M. Karlsson, M. Bartsch, and S. Raghavan, “Piezospectroscopic evaluation and damage identification for thermal barrier coatings subjected to simulated engine environments,” *Surface and Coatings Technology*, vol. 323, pp. 30–38, 2017.

[4] I. Hanhan, E. Durnberg, G. Freihofer, P. Akin, and S. Raghavan, “Portable piezospectroscopy system: non-contact in-situ stress sensing through high resolution photo-luminescent mapping,” *Journal of Instrumentation*, vol. 9, no. 11, p. P11005, 2014.

[5] A. L. Stevenson, *Calibration of alumina-epoxy nanocomposites using piezospectroscopy for the development of stress-sensing adhesives*. PhD thesis, University of Central Florida, 2011.

[6] J. C. Williams and E. A. Starke, “Progress in structural materials for aerospace systems,” *Acta Materialia*, vol. 51, no. 19, pp. 5775–5799, 2003.

[7] C. Soutis, “Carbon fiber reinforced plastics in aircraft construction,” *Materials Science and Engineering: A*, vol. 412, no. 1, pp. 171–176, 2005.

[8] C. Manjunatha, R. Bojja, N. Jagannathan, A. Kinloch, and A. Taylor, “Enhanced fatigue behavior of a glass fiber reinforced hybrid particles modified epoxy nanocomposite under wisperx spectrum load sequence,” *International Journal of Fatigue*, vol. 54, pp. 25–31, 2013.

[9] Y. Zheng, R. Ning, and Y. Zheng, “Study of sio2 nanoparticles on the improved performance of epoxy and fiber composites,” *Journal of Reinforced Plastics and Composites*, vol. 24, no. 3, pp. 223–233, 2005.

[10] M. Hussain, A. Nakahira, and K. Niihara, “Mechanical property improvement of carbon fiber reinforced epoxy composites by Al_2O_3 filler dispersion,” *Materials Letters*, vol. 26, no. 3, pp. 185–191, 1996.

[11] A. Mohanty, V. K. Srivastava, and P. U. Sastry, “Investigation of mechanical properties of alumina nanoparticle-loaded hybrid glass/carbon-fiber-reinforced epoxy composites,” *Journal of Applied Polymer Science*, vol. 131, no. 1, pp. 1–7, 2014.

[12] A. Alva and S. Raja, “Dynamic characteristics of epoxy hybrid nanocomposites,” *Journal of Reinforced Plastics and Composites*, vol. 30, no. 22, pp. 1857–1867, 2011.

[13] S. Raghavan, A. Stevenson, and A. Jones, “Stress-sensitive material and methods for using same,” tech. rep., US Patent, Sept. 28 2012. US Patent App. 13/630,236.

[14] A. Stevenson, A. Jones, and S. Raghavan, “Stress-sensing nanomaterial calibrated with photostimulated luminescence emission,” *Nano letters*, vol. 11, no. 8, pp. 3274–3278, 2011.

[15] G. Freihofer, D. Fugon-Dessources, E. Ergin, A. Van Newkirk, A. Gupta, S. Seal, A. Schu?lzgen, and S. Raghavan, “Piezospectroscopic measurements capturing the evolution of plasma spray-coating stresses with substrate loads,” *ACS Applied Materials & Interfaces*, vol. 6, no. 3, pp. 1366–1369, 2014.

[16] J. Barnett, S. Block, and G. Piermarini, “An optical fluorescence system for quantitative pressure measurement in the diamond-anvil cell,” *Review of Scientific Instruments*, vol. 44, no. 1, pp. 1–9, 1973.

[17] Q. Ma and D. R. Clarke, “Piezospectroscopic determination of residual stresses in polycrystalline alumina,” *Journal of the American Ceramic Society*, vol. 77, no. 2, pp. 298–302, 1994.

[18] S. Raghavan and P. K. Imbrie, “Ex-situ stress measurements in polycrystalline ceramics using photo-stimulated luminescence spectroscopy and high-energy x-rays,” *Journal of the American Ceramic Society*, vol. 92, no. 7, pp. 1567–1573, 2009.

[19] D. R. Clarke and D. J. Gardiner, “Recent advances in piezospectroscopy,” *International Journal of Materials Research*, vol. 98, no. 8, pp. 756–762, 2007.

[20] N. Muraki, N. Matoba, T. Hirano, and M. Yoshikawa, “Determination of thermal stress distribution in a model microelectronic device encapsulated with alumina filled epoxy resin using fluorescence spectroscopy,” *Polymer*, vol. 43, no. 4, pp. 1277–1285, 2002.

[21] J. Nychka and D. Clarke, “Damage quantification in tbcs by photo-stimulated luminescence spectroscopy,” *Surface and Coatings Technology*, vol. 146, pp. 110–116, 2001.

[22] S. Raghavan and P. Imbrie, “The development of photo-stimulated luminescence spectroscopy for 3d stress measurements in the thermally grown oxide layer of thermal barrier coatings,” *MATERIALS SCIENCE AND TECHNOLOGY-ASSOCIATION FOR IRON AND STEEL TECHNOLOGY-*, vol. 3, p. 2028, 2007.

[23] S. Sridharan, L. Xie, E. H. Jordan, and M. Gell, “Stress variation with thermal cycling in the thermally grown oxide of an eb-pvd thermal barrier coating,” *Surface and Coatings Technology*, vol. 179, no. 2, pp. 286–296, 2004.

[24] M. Gell, S. Sridharan, M. Wen, and E. H. Jordan, "Photoluminescence piezospectroscopy: A multi-purpose quality control and ndi technique for thermal barrier coatings," *International Journal of Applied Ceramic Technology*, vol. 1, no. 4, pp. 316–329, 2004.

[25] G. Freihofer, J. Dustin, H. Tat, A. Schülzgen, and S. Raghavan, "Stress and structural damage sensing piezospectroscopic coatings validated with digital image correlation," *AIP Advances*, vol. 5, no. 3, p. 037139, 2015.

[26] A. P. Selimov, R. Hoover, Q. Fouliard, A. C. Manero, P. Dackus, D. Carolan, A. Taylor, and S. Raghavan, "Characterization of hybrid carbon fiber composites using photoluminescence spectroscopy," in *58th AIAA/ASCE/AHS/ASC Structures, Structural Dynamics, and Materials Conference*, p. 0123, 2017.

[27] T. Hsieh, A. Kinloch, K. Masania, J. S. Lee, A. Taylor, and S. Sprenger, "The toughness of epoxy polymers and fibre composites modified with rubber microparticles and silica nanoparticles," *Journal of Materials Science*, vol. 45, no. 5, pp. 1193–1210, 2010.

[28] H. Khare and D. Burris, "A quantitative method for measuring nanocomposite dispersion," *Polymer*, vol. 51, no. 3, pp. 719–729, 2010.

[29] J. He and D. R. Clarke, "Determination of the piezospectroscopic coefficients for chromium-doped sapphire," *Journal of the American Ceramic Society*, vol. 78, no. 5, pp. 1347–1353, 1995.

[30] P. J. Clark and F. C. Evans, "Distance to nearest neighbor as a measure of spatial relationships in populations," *Ecology*, vol. 35, no. 4, pp. 445–453, 1954.

[31] V. Kushvaha and H. Tippur, "Effect of filler shape, volume fraction and loading rate on dynamic fracture behavior of glass-filled epoxy," *Composites Part B: Engineering*, vol. 64, pp. 126–137, 2014.

[32] E. Vassileva and K. Friedrich, "Epoxy/alumina nanoparticle composites. ii. influence of silane coupling agent treatment on mechanical performance and wear resistance," *Journal of Applied Polymer Science*, vol. 101, no. 6, pp. 4410–4417, 2006.

[33] M. E. Mackay, A. Tuteja, P. M. Duxbury, C. J. Hawker, B. Van Horn, Z. Guan, G. Chen, and R. Krishnan, "General strategies for nanoparticle dispersion," *Science*, vol. 311, no. 5768, pp. 1740–1743, 2006.

[34] S. Shokoohi, A. Arefazar, and R. Khosrokhavar, "Silane Coupling Agents in Polymer-based Reinforced Composites: A Review," *Journal of Reinforced Plastics and Composites*, vol. 27, no. 5, pp. 473–485, 2008.

[35] Z. Guo, T. Pereira, O. Choi, Y. Wang, and H. T. Hahn, "Surface functionalized alumina nanoparticle filled polymeric nanocomposites with enhanced mechanical properties," *Journal of Materials Chemistry*, vol. 16, no. 27, p. 2800, 2006.

[36] E. P. Plueddemann, "Adhesion Through Silane Coupling Agents," *The Journal of Adhesion*, vol. 2, no. 3, pp. 184–201, 1970.

[37] E. Vassileva and K. Friedrich, "Epoxy/alumina nanoparticle composites. ii. influence of silane coupling agent treatment on mechanical performance and wear resistance," *Journal of Applied Polymer Science*, vol. 101, no. 6, pp. 4410–4417, 2006.

[38] Z. Demjén, B. Pukánszky, and J. Nagy, "Evaluation of interfacial interaction in polypropylene/surface treated $CaCO_3$ composites," *Composites Part A: Applied Science and Manufacturing*, vol. 29, no. 3, pp. 323–329, 1998.

[39] I. A. Hanhan, *Hybrid Carbon Fiber Alumina Nanocomposite for Non-Contact Stress Sensing Via Piezospectroscopy*. PhD thesis, University of Central Florida Orlando, Florida, 2015.

[40] J. He, I. J. Beyerlein, and D. R. Clarke, “Load transfer from broken fibers in continuous fiber al_2o_3-al composites and dependence on local volume fraction,” *Journal of the Mechanics and Physics of Solids*, vol. 47, no. 3, pp. 465–502, 1999.

[41] G. Freihofer, *Nanocomposite coating mechanics via piezospectroscopy*. PhD thesis, University of Central Florida Orlando, Florida, 2014.

[42] D. J. Bray, S. G. Gilmour, F. J. Guild, and A. C. Taylor, “Quantifying nanoparticle dispersion by using the area disorder of delaunay triangulation,” *Journal of the Royal Statistical Society: Series C (Applied Statistics)*, vol. 61, no. 2, pp. 253–275, 2012.

[43] X. L. Ji, J. K. Jing, W. Jiang, and B. Z. Jiang, “Tensile modulus of polymer nanocomposites,” *Polymer Engineering & Science*, vol. 42, no. 5, pp. 983–993, 2002.

[44] A. Slipenyuk, V. Kuprin, Y. Milman, J. Spowart, and D. Miracle, “The effect of matrix to reinforcement particle size ratio (psr) on the microstructure and mechanical properties of a p/m processed alcumn/sicp mmc,” *Materials Science and Engineering: A*, vol. 381, no. 1, pp. 165–170, 2004.

[45] J. D. Barnett, S. Block, and G. J. Piermarini, “An optical fluorescence system for quantitative pressure measurement in the diamond-anvil cell,” *Review of Scientific Instruments*, vol. 44, no. 1, pp. 1–9, 1973.

[46] R. J. Christensen, D. M. Lipkin, and D. R. Clarke, “Nondestructive evaluation of the oxidation stresses through thermal barrier coatings using Cr^{3+} piezospectroscopy,” *Applied Physics Letters*, vol. 69, p. 3754, 1996.

[47] G. Freihofer, J. Dustin, H. Tat, A. Schülzgen, and S. Raghavan, “Stress and structural damage sensing piezospectroscopic coatings validated with digital image correlation,” *AIP Advances*, vol. 5, no. 3, p. 037139, 2015.

[48] B. Henderson and G. F. Imbusch, *Optical spectroscopy of inorganic solids*, vol. 44. Oxford University Press, 2006.

[49] D. Dragoman and M. Dragoman, *Optical characterization of solids*. Springer Science & Business Media, 2013.

[50] H. Hough, J. Demas, T. Williams, and H. Wadley, "Luminescence sensing of stress in ti/al 2 o 3 fiber reinforced composites," *Acta Metallurgica et Materialia*, vol. 43, no. 2, pp. 821–834, 1995.

[51] S. E. Molis and D. R. Clarke, "Measurement of stresses using fluorescence in an optical microprobe: Stresses around indentations in a chromium-doped sapphire," *Journal of the American Ceramic Society*, vol. 73, no. 11, pp. 3189–3194, 1990.

[52] A. Schawlow, *Advances in Quantum Electronics*, ch. Fine structure and properties of chromium fluorescence in aluminum and magnesium oxide, p. 50. Columbia University Press, New York, 1961.

[53] E. Feher and M. Sturge, "Effect of stress on the trigonal splittings of d 3 ions in sapphire (α-al 2 o 3)," *Physical Review*, vol. 172, no. 2, p. 244, 1968.

[54] R. A. Forman, G. J. Piermarini, J. D. Barnett, and S. Block, "Pressure measurement made by the utilization of ruby sharp-line luminescence," *Science*, vol. 176, no. 4032, pp. 284–285, 1972.

[55] G. Freihofer, A. Schülzgen, and S. Raghavan, "Multiscale mechanics to determine nanocomposite elastic properties with piezospectroscopy," *Acta Materialia*, vol. 81, pp. 211–218, 2014.

[56] S. Raghavan, P. K. Imbrie, and W. A. Crossley, “Spectral analysis of R-lines and vibronic sidebands in the emission spectrum of ruby using genetic algorithms,” *Applied Spectroscopy*, vol. 62, no. 7, pp. 759–765, 2008.

[57] G. Wertheim, M. Butler, K. West, and D. Buchanan, “Determination of the gaussian and lorentzian content of experimental line shapes,” *Review of Scientific Instruments*, vol. 45, no. 11, pp. 1369–1371, 1974.

[58] A. Selcuk and A. Atkinson, “Analysis of the cr 3+ luminescence spectra from thermally grown oxide in thermal barrier coatings,” *Materials Science and Engineering: A*, vol. 335, no. 1, pp. 147–156, 2002.

[59] M. Yourdkhani and P. Hubert, “Quantitative dispersion analysis of inclusions in polymer composites,” *ACS applied materials & interfaces*, vol. 5, no. 1, pp. 35–41, 2012.

[60] C.-J. Chang, L. Xu, Q. Huang, and J. Shi, “Quantitative characterization and modeling strategy of nanoparticle dispersion in polymer composites,” *IIE Transactions*, vol. 44, no. 7, pp. 523–533, 2012.

[61] D. Bray, S. Gilmour, F. Guild, T. Hsieh, K. Masania, and A. Taylor, “Quantifying nanoparticle dispersion: application of the delaunay network for objective analysis of sample micrographs,” *Journal of Materials Science*, vol. 46, no. 19, pp. 6437–6452, 2011.

[62] I. Hanhan, A. Selimov, D. Carolan, A. Taylor, and S. Raghavan, “Characterizing mechanical properties of hybrid alumina carbon fiber composites with piezospectroscopy,” in *57th AIAA/ASCE/AHS/ASC Structures, Structural Dynamics, and Materials Conference*, p. 1413, 2016.

[63] D. Bray, P. Dittanet, F. Guild, A. Kinloch, K. Masania, R. Pearson, and A. Taylor, “The modelling of the toughening of epoxy polymers via silica nanoparticles: the effects of volume fraction and particle size,” *Polymer*, vol. 54, no. 26, pp. 7022–7032, 2013.

[64] S. Zunjarrao, R. Sriraman, and R. Singh, “Effect of processing parameters and clay volume fraction on the mechanical properties of epoxy-clay nanocomposites,” *Journal of Materials Science*, vol. 41, no. 8, pp. 2219–2228, 2006.

[65] M. H. Wichmann, J. Sumfleth, F. H. Gojny, M. Quaresimin, B. Fiedler, and K. Schulte, “Glass-fibre-reinforced composites with enhanced mechanical and electrical properties–benefits and limitations of a nanoparticle modified matrix,” *Engineering Fracture Mechanics*, vol. 73, no. 16, pp. 2346–2359, 2006.

[66] I. Isik, U. Yilmazer, and G. Bayram, “Impact modified epoxy/montmorillonite nanocomposites: synthesis and characterization,” *Polymer*, vol. 44, no. 20, pp. 6371–6377, 2003.

[67] Z. Demjén, B. Pukánszky, and J. Nagy, “Evaluation of interfacial interaction in polypropylene/surface treated caco$_3$ composites,” *Composites Part A: Applied Science and Manufacturing*, vol. 29, no. 3, pp. 323–329, 1998.

[68] Y. Xu and S. Van Hoa, “Mechanical properties of carbon fiber reinforced epoxy/clay nanocomposites,” *Composites Science and Technology*, vol. 68, no. 3, pp. 854–861, 2008.

[69] Z. Guo, T. Pereira, O. Choi, Y. Wang, and H. T. Hahn, “Surface functionalized alumina nanoparticle filled polymeric nanocomposites with enhanced mechanical properties,” *Journal of Materials Chemistry*, vol. 16, no. 27, pp. 2800–2808, 2006.

[70] K. Gadkaree, “Particulate-fibre-reinforced glass matrix hybrid composites,” *Journal of materials science*, vol. 27, no. 14, pp. 3827–3834, 1992.

[71] A. Mohanty, V. K. Srivastava, and P. U. Sastry, "Investigation of mechanical properties of alumina nanoparticle-loaded hybrid glass/carbon-fiber-reinforced epoxy composites," *Journal of Applied Polymer Science*, vol. 131, no. 1, 2014.

[72] J. Long, X. Qin, and G. Wang, "Influence of surface energy on the elastic compression of nanosphere," *Journal of Applied Physics*, vol. 117, no. 5, p. 054310, 2015.

[73] S. F. Ferdous, M. F. Sarker, and A. Adnan, "Role of nanoparticle dispersion and filler-matrix interface on the matrix dominated failure of rigid c 60-pe nanocomposites: A molecular dynamics simulation study," *Polymer*, vol. 54, no. 10, pp. 2565–2576, 2013.

[74] E. P. Plueddemann, *Silane Coupling Agents*. New York; London: Plenum Press, 2nd ed. ed., 1991.

[75] S. Sterman and J. G. Marsden, "Silane coupling agents," *Industrial & Engineering Chemistry*, vol. 58, no. 3, pp. 33–37, 1966.

[76] J. R. Condon and J. L. Ferracane, "Reduced polymerization stress through non-bonded nanofiller particles," *Biomaterials*, vol. 23, no. 18, pp. 3807–3815, 2002.

[77] E. P. Plueddemann and G. Fanger, "Epoxyorganosiloxanes," *Journal of the American Chemical Society*, vol. 81, no. 11, pp. 2632–2635, 1959.

[78] S. Y. Fu, X. Q. Feng, B. Lauke, and Y. W. Mai, "Effects of particle size, particle/matrix interface adhesion and particle loading on mechanical properties of particulate-polymer composites," *Composites Part B: Engineering*, vol. 39, no. 6, pp. 933–961, 2008.

[79] J. R. Condon and J. L. Ferracane, "Reduced polymerization stress through non-bonded nanofiller particles," *Biomaterials*, vol. 23, no. 18, pp. 3807–3815, 2002.

[80] Infrastructure Nanomaterials, Manchester, CT 06042, *α - Aluminum Oxide (Alumina) nano powder, 99.8%, 40 nm grain size, APS 150 nm.*

[81] J. Kim, M. Kim, and K. Ha, “New ultrasonic dispersion method for nanoparticles using cylindrical piezoelectric transducer,” in *Ultrasonics Symposium (IUS), 2010 IEEE*, pp. 2072–2075, IEEE, 2010.

[82] Gurit, Wattwil, Switzerland, *UT-C400 Uni-directional Reinforcement Fabric datasheet*.

[83] T. Hsieh, A. Kinloch, K. Masania, J. S. Lee, A. Taylor, and S. Sprenger, “The toughness of epoxy polymers and fibre composites modified with rubber microparticles and silica nanoparticles,” *Journal of Materials Science*, vol. 45, no. 5, pp. 1193–1210, 2010.

[84] J. Wang, “A machinability study of polymer matrix composites using abrasive waterjet cutting technology,” *Journal of Materials Processing Technology*, vol. 94, no. 1, pp. 30–35, 1999.

[85] A. Standard *et al.*, “Standard test method for tensile properties of polymer matrix composite materials,” *ASTM D3039/D 3039M*, 2008.

[86] D. McCumber and M. Sturge, “Linewidth and temperature shift of the r lines in ruby,” *Journal of Applied Physics*, vol. 34, no. 6, pp. 1682–1684, 1963.

[87] R. Munro, G. Piermarini, S. Block, and W. Holzapfel, “Model line-shape analysis for the ruby r lines used for pressure measurement,” *Journal of Applied Physics*, vol. 57, no. 2, pp. 165–169, 1985.

[88] W. D. Callister and D. G. Rethwisch, *Materials science and engineering*, vol. 5. John Wiley & Sons NY, 2011.

[89] O. Prejzek, M. Španiel, and T. Mareš, “Microstructural residual stress in particle-filled dental composite,” *Computer Methods in Biomechanics and Biomedical Engineering*, vol. 18, no. 2, pp. 124–129, 2015.

[90] R. R. Braga, R. Y. Ballester, and J. L. Ferracane, "Factors involved in the development of polymerization shrinkage stress in resin-composites: a systematic review," *Dental Materials*, vol. 21, no. 10, pp. 962–970, 2005.

[91] C. Davidson and A. Feilzer, "Polymerization shrinkage and polymerization shrinkage stress in polymer-based restoratives," *Journal of Dentistry*, vol. 25, no. 6, pp. 435–440, 1997.

[92] B. Pukánszky, "Interfaces and interphases in multicomponent materials: past, present, future," *European Polymer Journal*, vol. 41, no. 4, pp. 645–662, 2005.

[93] K. S. Wilson and J. M. Antonucci, "Interphase structure–property relationships in thermoset dimethacrylate nanocomposites," *Dental Materials*, vol. 22, no. 11, pp. 995–1001, 2006.

[94] L. Chen, H. Jin, Z. Xu, M. Shan, X. Tian, C. Yang, Z. Wang, and B. Cheng, "A design of gradient interphase reinforced by silanized graphene oxide and its effect on carbon fiber/epoxy interface," *Materials Chemistry and Physics*, vol. 145, no. 1, pp. 186–196, 2014.

[95] D. Renusch, M. Grimsditch, I. Koshelev, B. Veal, and P. Hou, "Strain determination in thermally-grown alumina scales using fluorescence spectroscopy," *Oxidation of Metals*, vol. 48, no. 5, pp. 471–495, 1997.

[96] G. Marom, S. Fischer, F. Tuler, and H. Wagner, "Hybrid effects in composites: conditions for positive or negative effects versus rule-of-mixtures behaviour," *Journal of Materials Science*, vol. 13, no. 7, pp. 1419–1426, 1978.

[97] H. S. Kim, S. I. Hong, and S. J. Kim, "On the rule of mixtures for predicting the mechanical properties of composites with homogeneously distributed soft and hard particles," *Journal of Materials Processing Technology*, vol. 112, no. 1, pp. 109–113, 2001.

[98] H. Bruck and B. Rabin, “Evaluating microstructural and damage effects in rule-of-mixtures predictions of the mechanical properties of ni-al2o3 composites,” *Journal of Materials Science*, vol. 34, no. 9, pp. 2241–2251, 1999.

[99] S. Tjong and Y. Meng, “Microstructural and mechanical characteristics of compatibilized polypropylene hybrid composites containing potassium titanate whisker and liquid crystalline copolyester,” *Polymer*, vol. 40, no. 26, pp. 7275–7283, 1999.